

## LA-UR-20-21911

Approved for public release; distribution is unlimited.

Title: ZND Verification Tests for Reactive Burn Models in FLAG

Author(s): Price, Matthew Anthony

Intended for: Report

Issued: 2020-02-26

---

**Disclaimer:**

Los Alamos National Laboratory, an affirmative action/equal opportunity employer, is operated by Triad National Security, LLC for the National Nuclear Security Administration of U.S. Department of Energy under contract 89233218CNA000001. By approving this article, the publisher recognizes that the U.S. Government retains nonexclusive, royalty-free license to publish or reproduce the published form of this contribution, or to allow others to do so, for U.S. Government purposes. Los Alamos National Laboratory requests that the publisher identify this article as work performed under the auspices of the U.S. Department of Energy. Los Alamos National Laboratory strongly supports academic freedom and a researcher's right to publish; as an institution, however, the Laboratory does not endorse the viewpoint of a publication or guarantee its technical correctness.

# ZND Verification Tests for Reactive Burn Models in FLAG

Matthew A. Price

## 1 Introduction

The ZND theory, named after Zeldovich, von Neumann, and Doering, provides a simple model for one-dimensional ideal steady-state detonation [1]. It assumes that the detonation wave front starts with a shock that is a discontinuous jump and is followed by a finite-length reaction zone. Reactive burn (also called reactive flow) models are based on ZND theory, as they model the shock initiation and detonation process with a finite reaction rate. The ZND wave propagation test is essentially the only available test case where an analytic solution exists for verification of reactive burn models in numerical codes. However, there are extensions and variants of the ZND test that have been devised for verification of multidimensional flows [2, 3, 4].

The objective of this work is to provide verification of the reactive burn models currently implemented in the Lagrangian hydrocode FLAG and investigate the influence of mesh resolution, artificial viscosity models, and the Arbitrary Lagrangian-Eulerian (ALE) Euler relaxer on the simulation results. The burn models of interest are the Wescott-Stewart-Davis (WSD) model [5], the Scaled Uniform Reactive Flow (SURF) model [6] (specifically with the SURFplus model extension [7]), and the Arrhenius shock temperature state dependent WSD (AWSO) model [8]. Previously, Ralph Menikoff has used ZND tests for verification of the SURF and SURFplus models in the Eulerian hydrocode xRAGE [9, 10]. The ZND tests here are somewhat different than the approach by Menikoff. In particular, we use a piston-driven ZND detonation wave (via a prescribed constant velocity boundary condition) in a Lagrangian framework whereas Menikoff had a ZND wave followed by a invariant rarefaction wave. The xRAGE simulations were carried out on uniform grids and adaptive mesh refinement (AMR) grids. Although AMR was recently implemented in FLAG and now fully functional for 2D simulations, it will not be evaluated with ZND tests at this time.

Some work has been done previously for validating the reactive burn models in FLAG. For example, the validation studies of SURF with shock-to-detonation (SDT) tests [11], cylinder tests, and gap-stick tests [12]. Further validation of the AWSO, WSD, and SURF models is described in [13] for SDT, multi-shock, cylinder, and corner-turning tests. Recently, a large parameter study with approximately twenty SDT tests was performed to validate the AWSO, WSD, SURF, and SURFplus models while also investigating mesh resolution and artificial viscosity settings [14]. To the best of our knowledge, the current work represents the first documented verification of these

burn models in FLAG. The reader should note that many of the tables and figures in this report use units of cm/g/ $\mu$ s, which are the default units for FLAG. However, some lengths and velocities are expressed in  $\mu$ m and mm/ $\mu$ s, respectively, which are typical units for detonation analyses.

## 2 ZND wave solution

To develop the ZND solutions we start with the reactive Euler equations. The detonation flow is assumed to be a single-phase continuum with a rate law for single-step irreversible kinetics. The one-dimensional conservation equations and the rate equation are:

$$\frac{\partial}{\partial t} \begin{bmatrix} \rho \\ \rho u \\ \rho(e + u^2/2) \\ \rho\lambda \end{bmatrix} + \frac{\partial}{\partial x} \begin{bmatrix} \rho u \\ \rho u^2 + p \\ \rho u(e + u^2/2 + p/\rho) \\ \rho u\lambda \end{bmatrix} = \begin{bmatrix} 0 \\ 0 \\ 0 \\ \rho R_\lambda \end{bmatrix} \quad (1)$$

where  $\rho$  is density,  $u$  is particle velocity,  $p$  is pressure,  $e$  is the specific internal energy,  $\lambda$  is the reaction progress variable, and  $R_\lambda = R(\rho, P, \lambda, \dots)$  is the rate law. These conservation equations can be transformed from the fixed laboratory reference frame to a steady traveling shock reference frame (i.e. of the detonation wave) through a Galilean transformation. In the steady shock frame no variable has a dependence on time and the partial differential equations become ordinary differential equations (ODEs). For more details refer to Powers [15] (chapter 12). The equations can be further simplified to a reduced non-conservative form which leads to the well-known Rankine-Hugoniot jump equations:

$$\text{mass:} \quad \rho_0 D = \rho(D - u) \quad (2)$$

$$\text{momentum:} \quad p - p_0 = \rho_0 u D \quad (3)$$

$$\text{energy:} \quad e_0 + p_0 v_0 + \frac{1}{2} D^2 = e + p v + \frac{1}{2} (D - u)^2 \quad (4)$$

where  $v$  is specific volume and  $D$  is the detonation/shock velocity. The subscript ‘0’ represents ambient state conditions. The Rankine-Hugoniot equations are used to relate states on either side of the shock wave (e.g. the ambient state to the CJ state) [1]. The equation for the Rayleigh line comes from combining eqns. 2 (mass) and 3 (momentum) to eliminate  $u$ :

$$\frac{p - p_0}{v - v_0} = -\rho_0^2 D^2. \quad (5)$$

The equation for the Hugoniot curve, which represents the locus of all possible shocked states, comes from combining eqns. 2 (mass), 3 (momentum), and 4 (energy) to eliminate  $u$  and  $D$ :

$$e - e_0 = \frac{1}{2} (p + p_0) (v_0 - v) \quad (6)$$

Evaluating the Hugoniot equation requires an equation of state (EOS),  $e = e(\rho, P, \lambda)$  for the material. Because the unreacted material (“reactants”) and reacted material (“products”) are modeled with separate EOSs, this requires an additional closure for the mixture EOS. For the ZND solutions and burn models investigated here, a pressure and temperature equilibrium between the materials is assumed.

In ZND theory, detonation wave starts with an infinitesimally thin shock which compresses the unreacted explosive at ambient state to the von Neumann (VN) spike point. The shock is followed by a finite length reaction zone which ends at the fully reacted Chapman-Jouget (CJ) state. The shock jump follows the Rayleigh line from the initial state through the CJ point to the VN spike. In  $P-v$  space the Rayleigh line has a slope proportional to  $-D^2$  (see eqn. 5). At this point the explosive is still unreacted ( $\lambda = 0$ ) so the VN spike lies on the reactants Hugoniot. The reaction then takes place, according to some rate law, at states along the Rayleigh line starting at the VN point and ending at the CJ state (with  $\lambda = 1$ ). This process is illustrated in the  $P-v$  plane in Figure 2.1. The requirement that the Rayleigh line be tangent to the products Hugoniot is how  $D_{CJ}$  is determined for the ZND solution.

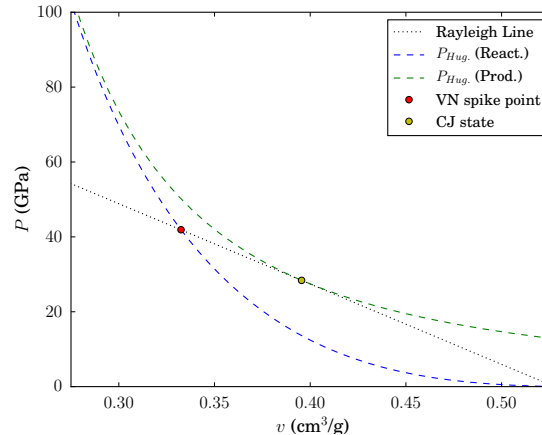


Figure 2.1:  $P - v$  Hugoniot and detonation jump condition for PBX 9502 with Davis EOSs.

For this work, we will only consider the explosive PBX 9502 (95% TATB and 5% Kel-F 800 by weight) at ambient temperature. ZND solvers use the Rankine-Hugoniot conditions to determine  $D_{CJ}$ , calculate the ZND spike point, then integrate the burn model reaction rate in time/space until reaching the CJ point. Due to the complexity of the analytic EOSs used with the burn models (e.g. the Davis EOSs), this requires an iterative procedure for solving the ODEs (as well as for the P-T closure). Consequently, the ZND solutions are semi-analytic rather than exact.

### 3 Reactive burn models and EOS

The WSD model is the oldest of the three burn models investigated (published in 2005 [5]). It builds on the earlier ignition and growth type models of Lee and Tarver [16]. WSD includes three terms:

an ignition term (hot spot formation), a fast reaction term (growth of hot spots to main reaction), and a slow reaction term (burn-out to completion), all of which are functions of the local pressure. The fast reaction term is further divided into “initiation growth” and “detonation growth”. WSD offers several improvements over ignition and growth models. It uses *tanh* functions based on shock density to smoothly transition between initiation and detonation regimes, and thereby avoids the discontinuous rate of ignition and growth. This separation of terms allows WSD to use a single calibration for both shock-to-detonation and detonation propagation problems. A function that is dependent on shock density ( $\rho_{SH}$ ) is used for switching between the initiation and detonation growth terms.

SURF was developed in 2010 [6] and SURFplus a little later [7]. It also builds on the ignition and growth model concepts. In particular, it is based on theory that hot-spots are activated by the shock front and subsequently grow and develop into burn fronts. The reaction progress variable in SURF is based on these effects and is a function of the shock pressure ( $P_{SH}$ ) and the local pressure. The shock pressure is determined from a special algorithm for detecting the lead shock [17]. The “plus” extension in SURFplus adds a second reaction rate for the slow carbon clustering reactions (e.g. in carbon rich TATB-based explosives). This requires an adjustment of the internal energy in the EOS based on the second reaction progress variable ( $\lambda_2$ ). This makes the code implementation of SURFplus notably different from WSD and AWSD (which only depend on the a single reaction progress variable,  $\lambda$ ). The SURFplus model implementation in FLAG utilizes the SURF rate and adds on the “plus” part. Therefore, verification of the SURFplus model also captures the SURF model.

AWSD is the newest of the burn models (published in 2018 [8]). The original idea behind AWSD was to develop a temperature dependent model that improved on WSD. Although it shares some similarities with WSD, there are also significant differences. The AWSD rate is dependent on the shock temperature ( $T_{SH}$ ) with Arrhenius-like rate terms. Approximation of the shock temperature is built into the main model algorithm, unlike the lead shock detection schemes of SURF. Like WSD, it uses smooth *tanh* functions to switch between rate terms. However, the overall rate form of AWSD is multiplicative and its rate terms represent fast-burn and slow burn-out instead of the specific shock-to-detonation and detonation propagation terms in WSD. AWSD also has a dependence on the local pressure like both WSD and SURF. Because AWSD rate is a function of shock temperature it has the unique ability for a single calibration to be used for a range of initial temperatures. As SURF and AWSD are both dependent on the shock state, they can naturally predict the corner turning phenomenon. The original form of WSD lacks this ability, but additional deadening terms were added in an effort to make the model predictive of dead zones and corner turning [18].

For burn model validation the EOS functional form and parameters used in a reactive burn model simulations should always be the same as those used for the burn model calibration. Likewise, it is essential for the ZND verification tests that the same EOSs that were used for generating the semi-analytic ZND profiles and are used in hydrocode simulations. All three models investigated

here are used with the so-called Davis EOSs for the reactants and products (described in [5] and [8]). Even though SURF is calibrated with different EOS forms, the ZND profile generated by Ralph Menikoff used the Davis EOSs, so for verification purposes the analytic ZND profile is consistent with the hydrocode simulations. The complete sets of rate and EOS parameters for each burn model are given in Appendices A, B, and C. In this report, discussion and results from the three burn models will be arranged according to the models' development order (i.e. WSD, SURFplus, AWSO).

## 4 ZND profiles

The ZND solutions for WSD and AWSO were generated with a double-precision Fortran code that used a 5th order Runge-Kutta method to integrate the ODEs along  $dx$ . The ZND profiles have a spatial resolution of  $1.0 \mu\text{m}$ . The initiation term in the WSD model causes a sub-micron length scale spike (for the region  $0 < \lambda < 0.025$ ), as shown in Figure 4.1. To resolve this, an initial step size of  $0.1 \mu\text{m}$  was used while  $\lambda < 0.05$  during integration. The SURFplus ZND solution was generated by Ralph Menikoff and has a spatial resolution of  $\sim 1.0 \mu\text{m}$  (integrated along  $d\lambda$ ). The ZND solution data were split into separate files for each variable, so they could be interpolated into FLAG simulations as 1D fields. When interpolated into FLAG, the ZND profiles do not include the detonation energy. This energy shift is added via a parameter in the products EOS.

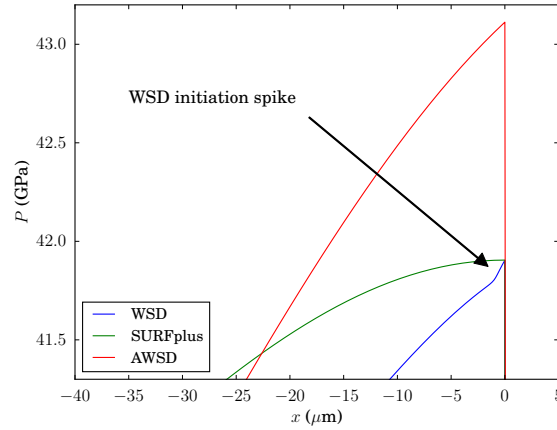


Figure 4.1: Zoom-in of ZND pressure profiles to show the spike in the WSD solution.

Calculating the ZND solution requires a assumed detonation velocity,  $D$ . Ideally, one would choose  $D$  which goes through the CJ-point (i.e.  $D_{CJ}$ ). However, determining the exact  $D_{CJ}$  can be challenging (root-finding to solve the Rankine-Hugoniot equations is more difficult as  $\lambda \rightarrow 1$ ) and often we assume a slightly higher value of  $D_{CJ}$ . The  $D_{CJ}$  for WSD was chosen to be similar to SURFplus. However, it is not exactly the same which accounts for the slight differences in the CJ state.  $D_{CJ}$  and corresponding reaction zone lengths,  $L_{rz}$ , for the burn models are given in Table 4.1.

Table 4.1:  $D_{CJ}$  and reaction zone length scales.

	$D_{CJ}$ (mm/ $\mu$ s)	$L_{rz}(\lambda = 0.5)$ ( $\mu$ m)	$L_{rz}(\lambda = 0.999)$ (mm)	$L_{rz}(\lambda \approx 1.0)$ (mm)
WSD	7.73150000	37.5	2.361	2.78220
SURFplus	7.73151082	37.7	2.480	2.51489
AWSD	7.80000000	24.7	4.176	10.5210

SURFplus has two reaction rates ( $\lambda$  and  $\lambda_2$ ) which makes determining these reaction zone lengths a little more complicated. In this case, the half-reaction zone length is inferred from the fast reaction,  $\lambda_1$ , and the total reaction zone length from  $\lambda_2$ . The AWSD reaction zone length is significantly longer than WSD and SURFplus due to the slow depletion of the burn-out part of the reaction rate. In practice, this can lead to longer run times for AWSD because there are typically more zones which are burning.

Profiles of the analytic ZND solutions from the three burn models are given in Figure 4.2 for the main variables and Figure 4.3 for the extra variables specific to the different models. Tables 4.2 - 4.4 list values from ZND solutions of the three burn models at the ambient, von-Neumann (shock), and CJ states. Note the differences in the ambient states between burn models. AWSD and WSD solutions start at the reference density of their respective reactants EOS and  $p_0 = 0.0$  Mbar. The SURFplus ZND solution starts at a pressure of  $p_0 = 10^{-6}$  Mbar (1 bar), which causes the ambient density and energy to differ slightly from the reference values.

Table 4.2: Ambient, von-Neumann, and CJ states for the WSD ZND solution.

Variable	Ambient	VN	CJ	Units
$\rho$	1.895	3.00764382	2.52847010	g/cm <sup>3</sup>
$p$	0.0	0.419050623	0.283795190	Mbar
$u$	0.0	0.286018099	0.193701086	cm/ $\mu$ s
$T$	293	1623.05305	3097.18894	K
$e$	0.0	0.0409031766	0.0187600554	Mbar-cm <sup>3</sup> /g
$\lambda$	0.0	0.0	1.0	
$\rho_{SH}$	1.895	3.00764382	3.00764382	g/cm <sup>3</sup>

Table 4.3: Ambient, von-Neumann, and CJ states for the SURFplus ZND solution.

Variable	Ambient	VN	CJ	Units
$\rho$	1.89505069	3.00765698	2.51758852	g/cm <sup>3</sup>
$p$	1.0e-06	0.419048039	0.280112258	Mbar
$u$	0.0	0.286007603	0.191181280	cm/ $\mu$ s
$T$	296.13	1631.34730	3084.65677	K
$e$	-3.57016376e-07	0.0409000126	0.0182749145	Mbar-cm <sup>3</sup> /g
$\lambda_1$	0.0	0.0	1.0	
$p_{SH}$	1.0e-06	0.419048039	0.419048039	Mbar
$\lambda_2$	0.0	0.0	1.0	



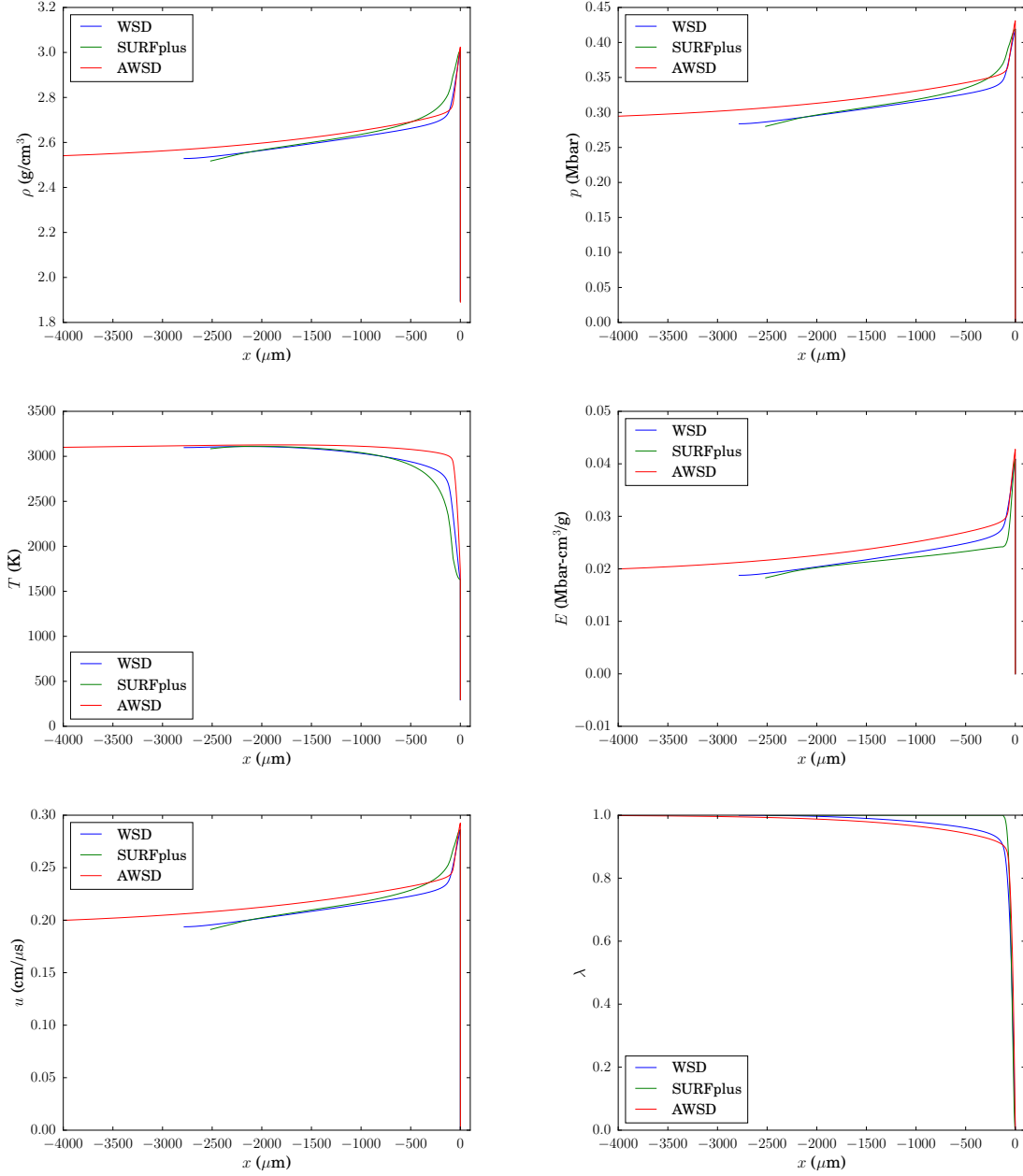


Figure 4.2: Analytic ZND profiles for the main variables in the three burn models.

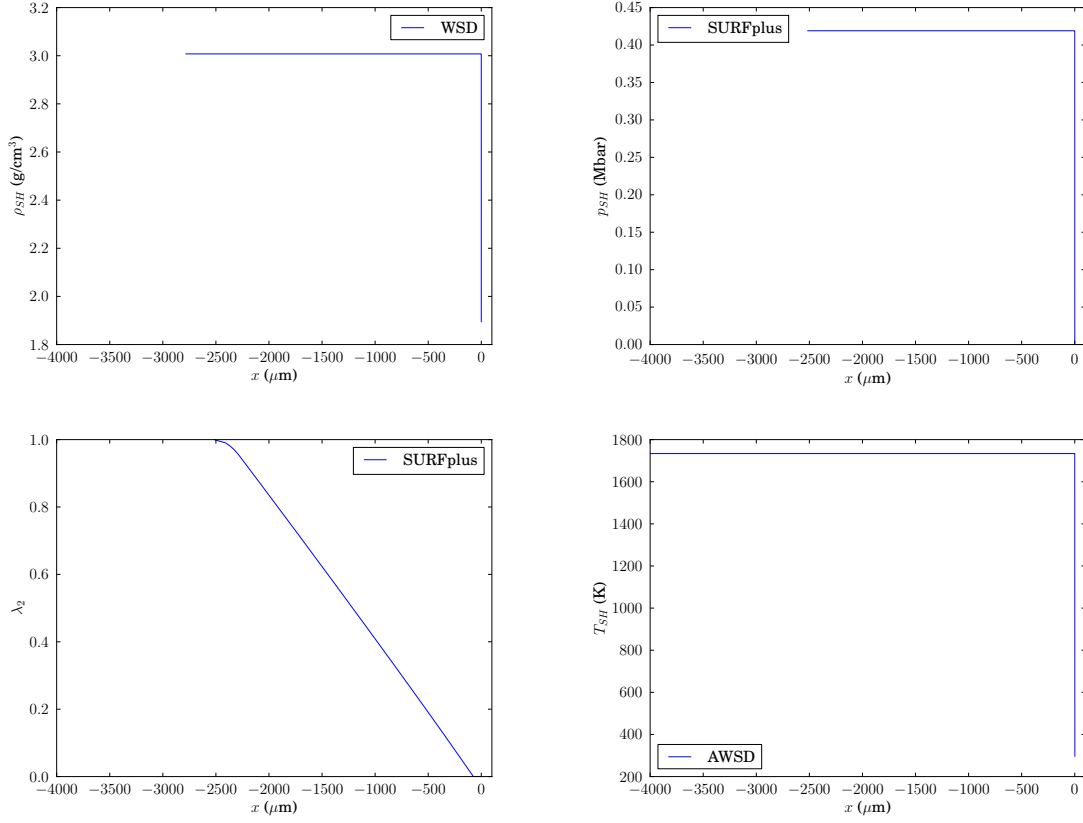


Figure 4.3: Analytic ZND profiles for extra variables in the three burn models.

Table 4.4: Ambient, von-Neumann, and CJ states for the AWSO ZND solution.

Variable	Ambient	VN	CJ	Units
$\rho$	1.890	3.02366003	2.52206354	$\text{g/cm}^3$
$p$	0.0	0.431122696	0.288174617	Mbar
$u$	0.0	0.292445188	0.195478644	$\text{cm}/\mu\text{s}$
$T$	297	1733.77883	3081.51692	K
$e$	0.0	0.0427620939	0.0191059501	$\text{Mbar}\cdot\text{cm}^3/\text{g}$
$T_{SH}$	297	1733.77883	1733.77883	K
$\lambda$	0.0	0.0	1.0	
$\zeta$	0.0	0.0	0.365259386	

## 5 Numerical simulations

This work uses a custom version of FLAG that is aligned with 3.8.Alpha.18 and was run with the CTSIfast suite on the Snow HPC cluster. There is non-released functionality that allows model parameter fields to be initialized from 1D files (i.e.  $T_{SH}$ ,  $P_{SH}$ ,  $\lambda_2$ , and  $\rho_{SH}$  - see Figure 4.3). This functionality will be included in future releases of FLAG. The simulations used the staggered-grid hydro (SGH) scheme [19]. The main set of verification tests were performed with the standard Lagrangian method, with some additional tests included to evaluate the Euler ALE relaxer.

The basic approach for running the FLAG ZND tests is as follows:

- Interpolate the semi-analytic ZND wave solution into a 1D FLAG simulation domain to initialize the density, energy, velocity, and burn fraction ( $\lambda$ ) fields. Similarly initialize fields for other model dependent variables (e.g.  $P_{SH}$  and  $\lambda_2$  for SURFplus).
- Prescribe a constant velocity boundary condition, at  $u_{CJ}$ , on the left side of the domain to provide a piston-supported steady detonation wave.
- Allow the detonation wave to propagate numerically for some sufficient amount of time according to the hydro scheme and burn model.
- Compare the simulation wave profiles with the analytic solution. The exact position of the shock with time is determined using the analytic detonation velocity.

### 5.1 Artificial viscosity

FLAG has several choices for artificial/shock viscosity (AV) models. AV models modify the momentum and energy conservation equations by adding dissipation with viscosity-like terms. This is necessary in hydrocode simulations to smear out shocks (numerical discontinuities) over several computational zones. The basic VNR model is based on the original quadratic functional form proposed by von-Neumann and Richtmeyer [20] with the additional linear term of Landshoff [21]. In FLAG, these terms are split further depending if the material is in compression or expansion. The total viscosity (pressure) is calculated as:

$$q = \begin{cases} q_1\rho(\Delta u)a + q_2\rho(\Delta u)^2 & \text{for compression,} \\ q_{1n}\rho(\Delta u)a + q_{2n}\rho(\Delta u)^2 & \text{for expansion,} \end{cases} \quad (7)$$

where  $q_1$  and  $q_{1n}$  are parameters for the linear term,  $q_2$  and  $q_{2n}$  are parameters for the quadratic term,  $a$  is the sound speed, and  $\Delta u$  is the change in velocity across the cell. A total of eight AV models/parameter sets were used in this study and are shown in Table 5.1. The goal is to understand how these models affect detonation wave propagation and identify model/parameter sets which are either recommended or discouraged for use (and the reasons why).

The VNR model in FLAG calculates a zone centered viscous pressure that depends on the zone length (1D), zone area (2D), or zone volume (3D). The Barton model [19] is based on a “fix” to

Table 5.1: Artificial viscosity models and parameter sets.

name:	<i>barton1</i>	<i>barton2</i>	<i>barton3</i>	<i>vnr1</i>	<i>mars1</i>	<i>mars2</i>	<i>mars3</i>	<i>bbl1</i>
model:	Barton	Barton	Barton	VNR	MARS	MARS	MARS	BBL
$q_1 =$	0.0	0.1	0.3	0.3	1.0	1.0	2.2	1.0
$q_{1n} =$	0.0	0.1	0.1	0.1	0.1	0.5	0.5	0.1
$q_2 =$	2.0	2.0	1.33	1.33	1.333	1.333	1.333	1.0
$q_{2n} =$	0.0	0.0	0.0	0.0	0.0	0.0	0.0	0.0

MARS models use `model_mars` = 2 and `bjfac` = 0.75.

BBL models use `length` = 2.

earlier AV models such that the viscosity force is calculated at the zone edge rather than the zone center [22, 23]. This allows calculations with large zonal aspect ratios (where VNR fails), but adds directionality because the viscous force lies along the direction of the relative velocity.

The *barton1* parameter set are the default values for the Barton model in FLAG and has been widely used. The choice of  $q_2 = 2$  is common for many solid materials and possibly has origins in the paper by Wilkins [24]. For *barton2*,  $q_1$  and  $q_{1n}$  are increased slightly for more dissipation. The *barton3* and *vnr1* sets have parameter values often used for gaseous materials and should work well for the explosive products.

MARS and BBL are more advanced AV models than VNR and Barton. MARS (the Multidimensional Approximate Riemann Solver) calculates shock viscosity from an approximate Riemann solver [25] which is based on the linear  $U-u$  relationship:

$$U = C_0 + su, \quad (8)$$

where  $U$  is shock velocity and  $C_0$  and  $s$  are fitting terms (intercept and slope). The MARS implementation in FLAG assumes a shock impedance of:

$$\mu = \rho U = \rho(a q_1 + q_2 \Delta u), \quad (9)$$

meaning that  $C_0 \equiv a q_1$  and  $s \equiv q_2$ . The *mars1* parameter set represents recommended values. Setting  $q_1 = 1$  ensures that the Riemann solver uses local sound speed as intended. The value of  $q_2 = 1.333$  is an estimate based on  $s$  values of common metals [26]. Figure 5.1 shows  $U-u$  Hugoniot curves for the PBX 9502 Davis EOSs and several linear  $U-u$  fits. Gustavsen et al. [27] determined a linear  $U-u$  Hugoniot fit for a large set of experimental data to be  $C_0 = 2.97$  mm/ $\mu$ s and  $s = 1.81$  with a range of  $0.8 \leq u \leq 2.3$  mm/ $\mu$ s (the vertical reference lines represent this data range). While this fit is quite close to the Davis  $U-u$  Hugoniot over the experimental data range, it deviates near the VN point. Three linear  $U-u$  Hugoniots are plotted for  $s = 1.333$  with  $C_0 = 1.75$  mm/ $\mu$ s (the ambient sound speed for PBX 9502),  $C_0 = 7.79$  mm/ $\mu$ s (sound speed at the VN point), and  $C_0 = 3.85$  mm/ $\mu$ s (which matches the data near the VN state). The idea behind the *mars3* parameter set, was to increase  $C_0$  by setting  $q_1 = 2.2$  and provide more dissipation for strong shocks (i.e. detonation). The difference between *mars1* and *mars2* is an increase in  $q_{1n}$  for

more dissipation in the expansion terms (for reasons that will be discussed in the results section).

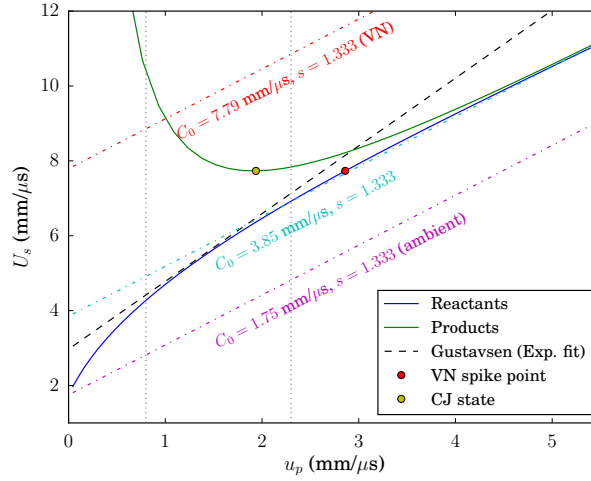


Figure 5.1: Hugoniot for PBX 9502 with Davis EOSs and some linear  $U-u$  fits.

BBL is a full tensor AV model using the mimetic approach developed by Brezzi, Buffa and Lipnikov [28]. BBL offers a symmetric and non-symmetric viscous model based on mimetic approximation of the  $\text{div}(\mu \nabla \mathbf{u})$  operator which has a form similar to physical viscosity. It enhances and extends capabilities of the Campbell-Shashkov tensor viscosity [29]. The advantage of tensor-based viscosity is that it is zone-centered and should be more accurate in cases of shear flow, but can be directionally dependent like an edge viscosity.

## 5.2 Simulation setup

A pseudo-1D domain was used for simulations (i.e. a 2D domain that is one zone thick) because MARS, BBL, and Euler-ALE require a 2D or 3D domain. The domain thickness is scaled with resolution so that zones have a uniform 1:1 aspect ratio. This is especially important for VNR because it is not suitable for large zonal aspect ratios (and can cause mesh tangling even in pseudo-1D) [22]. The left side of the domain is set to match the length of the ZND profile ( $x_{lft} = -L_{rz}(\lambda \approx 1.0)$ , refer to Table 4.1) with the shock initially located at  $x = 0$ . The right side of the domain was  $x_{rht} = 6.0$  cm. Simulation stopping time is set so that the ZND wave does not reach the right boundary:

$$t_{\text{stop}} = 0.8 (x_{rht}) / D_{CJ}. \quad (10)$$

The ZND semi-analytic solution fields are read into FLAG using the `interp_1D` capability. The density and energy are used to initialize the explosive material,  $\lambda$  is used to initialize the burn fraction field, and velocity is used to set the initial velocity field. The CJ velocity is also used to set the velocity boundary condition at  $x_{lft}$ . The initialized profile is nearly discontinuous and will smear out over several computational zones during the first few time steps of the simulations. This leads to small “start-up errors” which are errors related to entropy generated from numerical

dissipation [30]. The simulations are run sufficiently long to avoid any effects of these errors. At  $t_{\text{stop}}$ , the simulated profiles are shifted back for comparison with the analytic solution via:

$$x' = x - t_{\text{stop}} D_{CJ}. \quad (11)$$

It is important to realize that this represents a snapshot of the unsteady numerical wave propagation. There is some variation in the simulated profiles at different times, especially at coarser resolutions.

### 5.3 Parameter studies

A mesh convergence study was conducted with resolutions of 256, 128, 64, 32, 16, 8, 4, and 2  $\mu\text{m}$ . In Lagrangian simulations, this represents the initial zone sizes which can become much smaller near the shock due to compression. Coarser mesh sizes ( $\geq 32 \mu\text{m}$ ) are commonly used in engineering-scale simulations while finer mesh sizes ( $< 32 \mu\text{m}$ ) are typically reserved for validation and convergence studies. The reader should note the terms “coarse” and “fine” are relative to the particular problem and explosive material. To get to asymptotic behavior of the models we need to resolve the smallest features of the detonation structure. For example, in AWSD this typically requires resolutions below the half reaction zone width so that  $T_{SH}$  can be reasonably approximated. With WSD, obtaining convergence for problems involving shock initiation may require resolving the sub-micron initiation spike shown in Figure 4.1 (but is not necessary for the ZND tests because it is a propagating detonation).

The complete simulation matrix consists of three burn models (WSD, SURFplus, and AWSD), eight mesh resolutions, and eight artificial viscosity models. This required roughly 200 FLAG simulations. Additional simulations were run to test the Euler ALE relaxer and some specific parameter variations outside the main study.

## 6 Summarized results for eight AV model sets

It would be onerous to present results for each variable ( $\rho$ ,  $p$ ,  $e$ , etc.) in the simulation matrix. Instead we present only the pressure profiles for each burn model and AV set to quickly draw some conclusions. The detonation wave profile and shock location are expected to converge to the analytic solution with increased mesh resolution. Results from the simpler Barton and VNR models are grouped together, as are results from the more advanced MARS and BBL models. Differences between AV models tend to be more obvious at coarse resolutions, so we will focus on results at zone sizes  $> 32 \mu\text{m}$ .

### 6.1 Barton and VNR

Figures 6.1 - 6.3 show results for Barton and VNR parameter sets for the three burn models. We observe similar trends between the different AV sets for the burn models. The *barton1* set

(i.e. Barton with default parameters) does not provide enough dissipation for the detonation wave and consequently there are very large oscillations near the shock. There are also very large undershoots behind the shock at coarse resolutions which is due to a lack of dissipation in expansion (because  $q_{1n} = 0$ ). WSD does particularly poorly with the *barton1* parameter at coarse resolutions. The *barton2* and *barton3* sets provide more dissipation and are generally quite similar, but the *barton3* set appears to have slightly better behavior at coarser resolutions. While the *vnr1* set has the same parameters as *barton3*, it seems to provide more dissipation and less undershooting in the rarefaction.

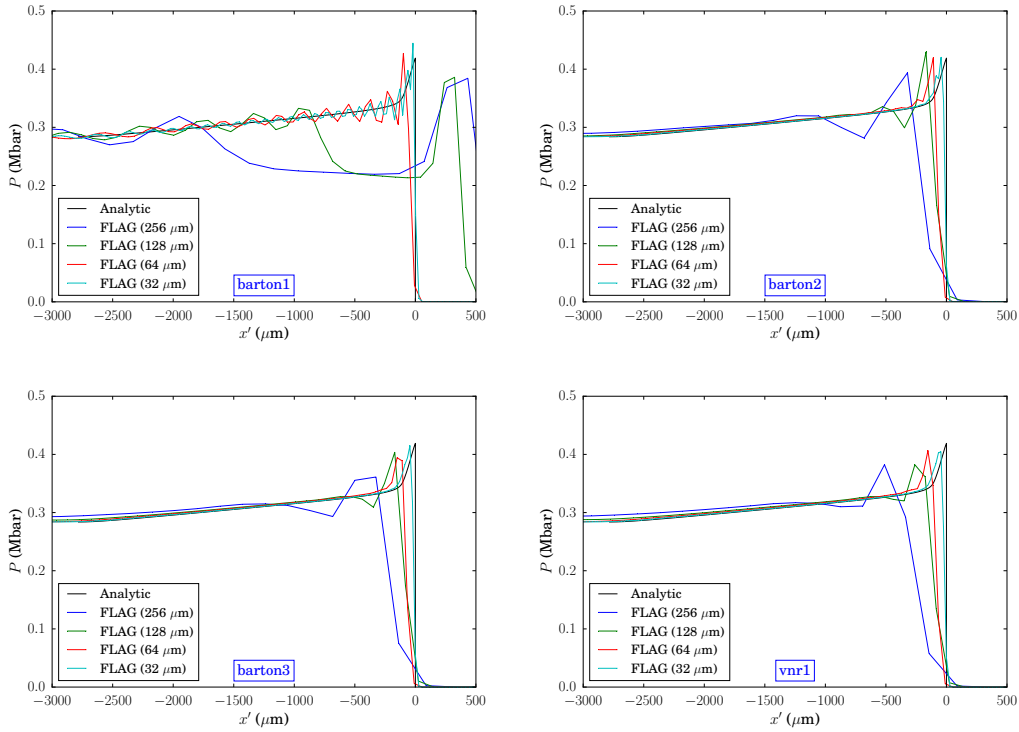


Figure 6.1: WSD pressure profiles with Barton and VNR.

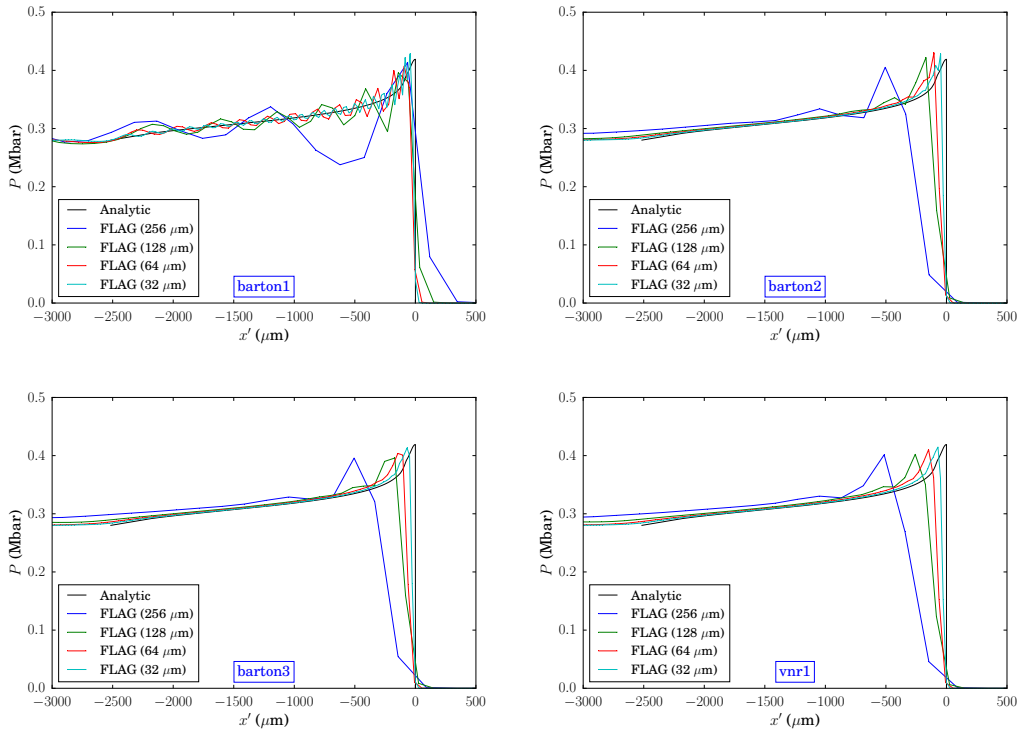


Figure 6.2: SURFplus pressure profiles with Barton and VNR.

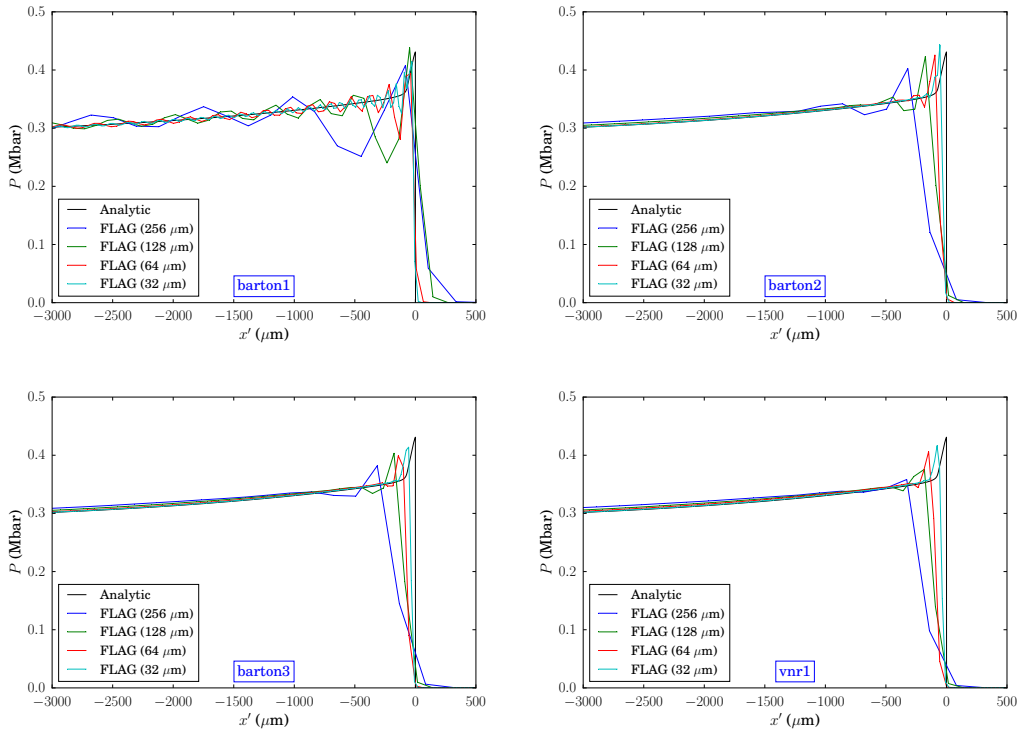


Figure 6.3: AWSO pressure profiles with Barton and VNR.



## 6.2 MARS and BBL

Figures 6.4 - 6.6 show results between the MARS and BBL parameter sets for the three burn models. The *mars1* set represents a “default” set of parameters commonly used with MARS. It is fairly compressive and the detonation wave tends to be ahead of other AV models (and the analytic solution) at coarser resolutions. There is also a very significant undershoot behind the shock front, which is primarily due to the lack of dissipation in expansion ( $q_{1n} = 0.1$ ). These undershoots can potentially contribute to EOS issues (especially during P-T equilibration of a partially reacted explosive material). Increasing the  $q_{1n}$  parameter to 0.5 in *mars2* dramatically improves this undershooting. The *mars3* results are generally similar to *mars2* at these coarser resolutions. A larger  $q_1$  does act to dampen oscillations at the finest resolutions ( $< 8 \mu\text{m}$ ). However, it is recommended that this value be left as  $q_1 = 1.0$  so that MARS utilizes the local sound speed for the Riemann solution as intended. Additional runs with MARS have shown that increasing  $q_2$  has a much smaller influence on the solutions, which may be inferred from eqn. 9 ( $a q_1 > q_2 \Delta u$ ). Results with the *bbl1* set appear to have more dissipation than the MARS sets, but still exhibit undershooting behind the shock at the coarsest resolution. Advantages of using the BBL tensor viscosity model will likely be realized with more complex 2D and 3D simulations, especially where there is curvature or diffraction of the detonation wave.

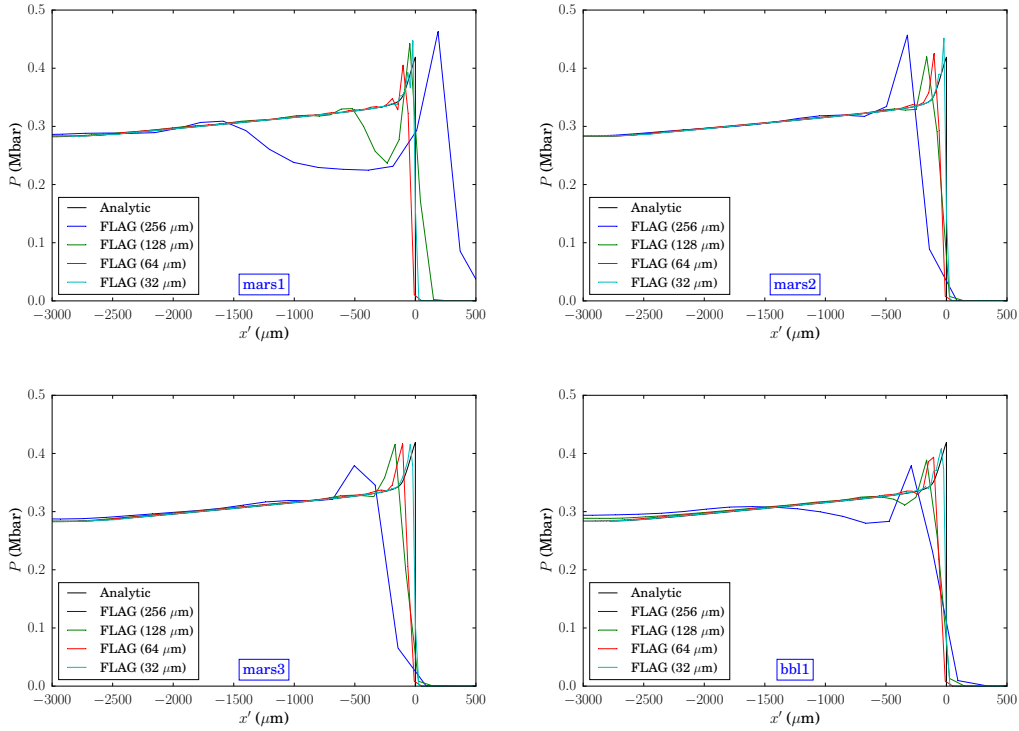


Figure 6.4: WSD pressure profiles with MARS and BBL.

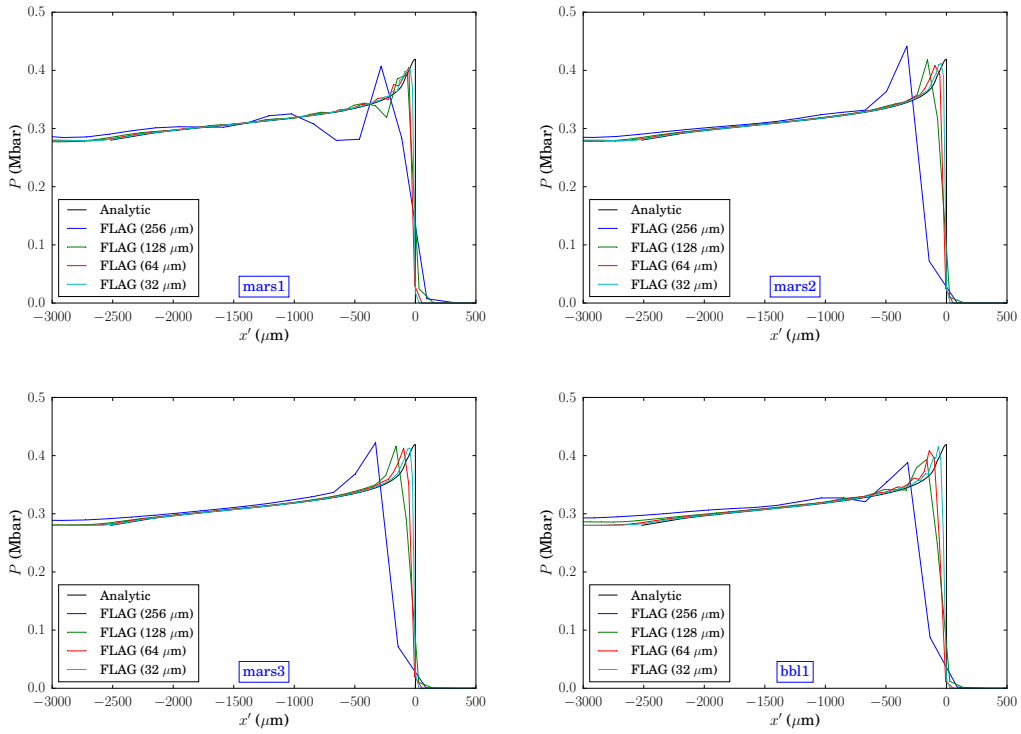


Figure 6.5: SURFplus pressure profiles with MARS and BBL.

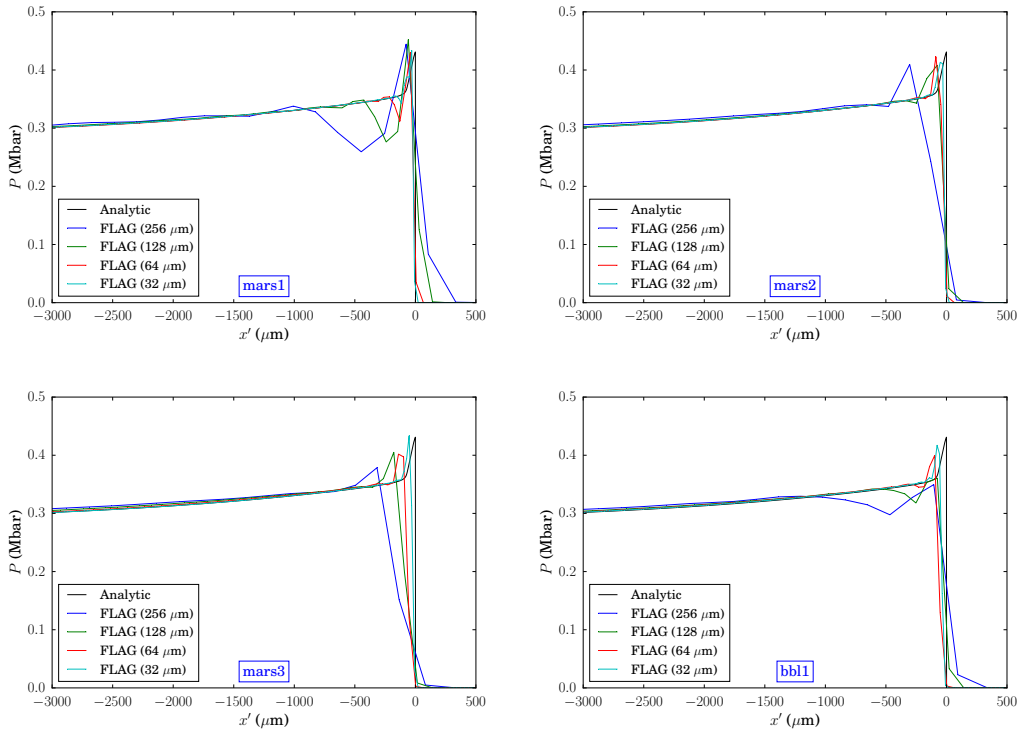


Figure 6.6: AWSO pressure profiles with MARS and BBL.

### 6.3 Detonation velocity convergence

In the previous figures all of the AV models appear to converge to the analytic solution (and thus  $D_{CJ}$ ) under resolution, but it is difficult to tell with certainty. Plotting the simulation detonation velocity ( $D_{\text{sim}}$ ) versus mesh resolution illustrates these trends more clearly, as shown in Figure 6.7. Calculating  $D_{\text{sim}}$  from reactive burn models is not always straightforward due to oscillations in the propagating detonation wave and build-up to steady detonation velocity (despite initializing with a fully-developed detonation profile). The best method we have found to determine  $D_{\text{sim}}$  is to track the shock arrival/position at every zone and then fit the slope of that  $x(t)$  curve to determine  $D_{\text{sim}}$ . Some early part of the solution domain ( $x < 3.0$  cm) is excluded to avoid the influence of numerical start-up errors. Subfigures in Figure 6.7 use the same range on the vertical axis (40 m/s) for comparison of burn models. Reference lines show the exact  $D_{CJ}$  values.

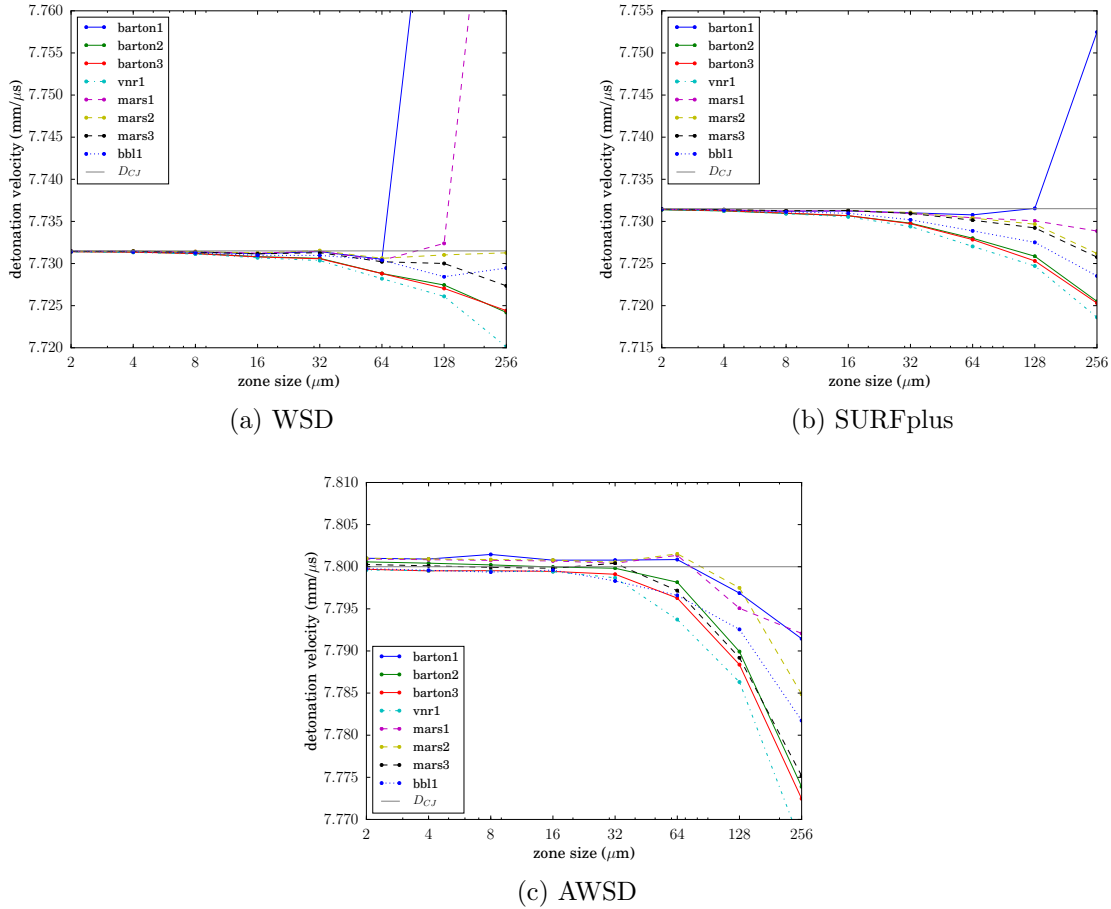


Figure 6.7:  $D_{\text{sim}}$  convergence under resolution for eight different AV sets (semi-log plots).

In general, all three burn models converge towards  $D_{CJ}$  as zone size decreases, regardless of the AV model. The variation in  $D_{\text{sim}}$  between AV sets (and error versus  $D_{CJ}$ ) is greater for coarser resolutions. This is particularly evident for WSD at zones sizes above  $64 \mu\text{m}$  and with the *barton1* AV set. FLAG users with poorly-resolved simulations should be mindful of this. Most models

tend to converge from below  $D_{CJ}$  (i.e. shocks are slightly behind of the analytic solution). At a  $16 \mu\text{m}$  zone size all models have nearly reached their converged value of  $D_{\text{sim}}$ . With increased mesh resolution, the calculated  $D_{\text{sim}}$  from WSD and SURFplus converge tightly to  $D_{CJ}$ , but AWSO shows a larger spread in  $D_{\text{sim}}$  (which is also sensitive to AV model choice). While this is noticeable in these convergence plots this spread is actually quite small ( $\sim \pm 1 \text{ m/s}$ ).

All three models have a dependence on shock state variables, and some of their convergence behavior may be explained by how well they capture the shock state with increased resolution. We start by looking at shock density in the WSD model, shown in Figure 6.8. The *barton1* AV set was intentionally chosen for this comparison because it causes large oscillations near the shock (a “worst” case). Under resolutions,  $\rho_{SH}$  actually converges to a value that is too high but this does not affect the  $D_{\text{sim}}$  convergence (see Figure 6.7). This is because  $\rho_{SH}$  essentially just controls a switching function in the WSD model rather than directly contributing to the rate. Next we look at shock pressure in the SURFplus model, shown in Figure 6.9, again with *barton1*. Even though there are significant oscillations in  $P_{SH}$ , the predicted values converge to the expected value. This speaks to the robustness of the lead shock detection algorithm even when AV model is overly compressive (such as with *barton1* and *mars1*).

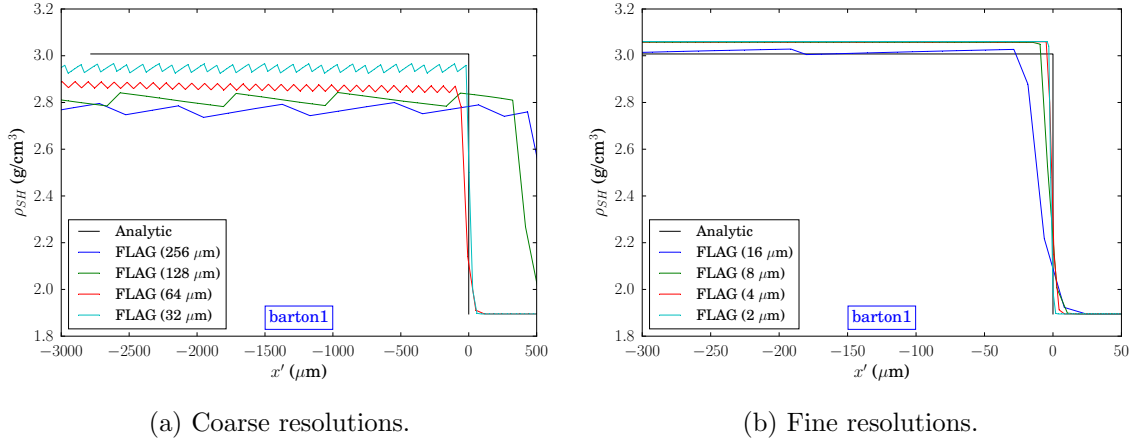


Figure 6.8: Convergence of shock density in WSD with *barton1*.

Approximating shock temperature for the AWSO model is more challenging than shock density in WSD or shock pressure in SURFplus. Unlike density and pressure which have maximum values at the shock, temperature increases behind the shock (see Figure 4.2). In AWSO, shock temperature is approximated as:

$$T_{SH} = \begin{cases} \max(\text{current } T_{SH}, T^*) & \text{if } \lambda < 1/2 \text{ and } \zeta < 1 \\ \text{current } T_{SH} & \text{otherwise,} \end{cases} \quad (12)$$

where  $\zeta$  is a timer progress variable and  $T^*$  is a function with a relative maximum at the shock

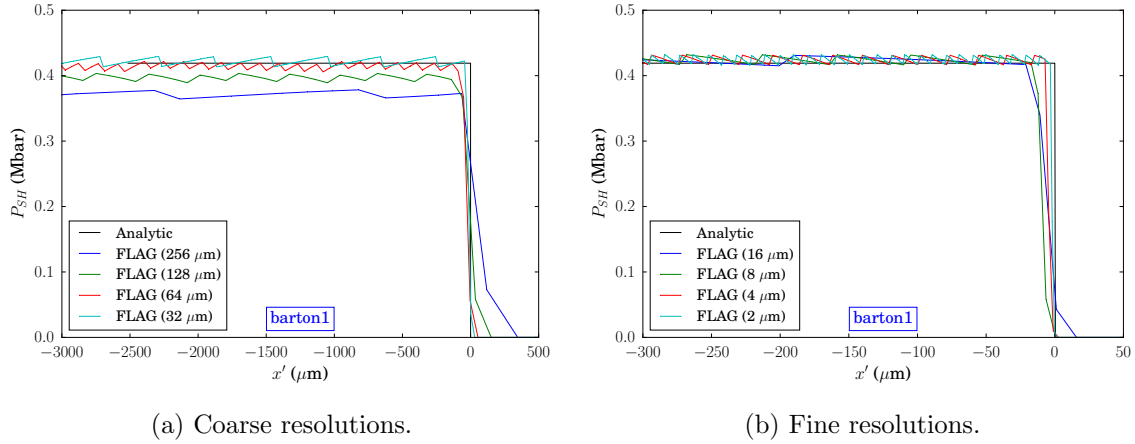
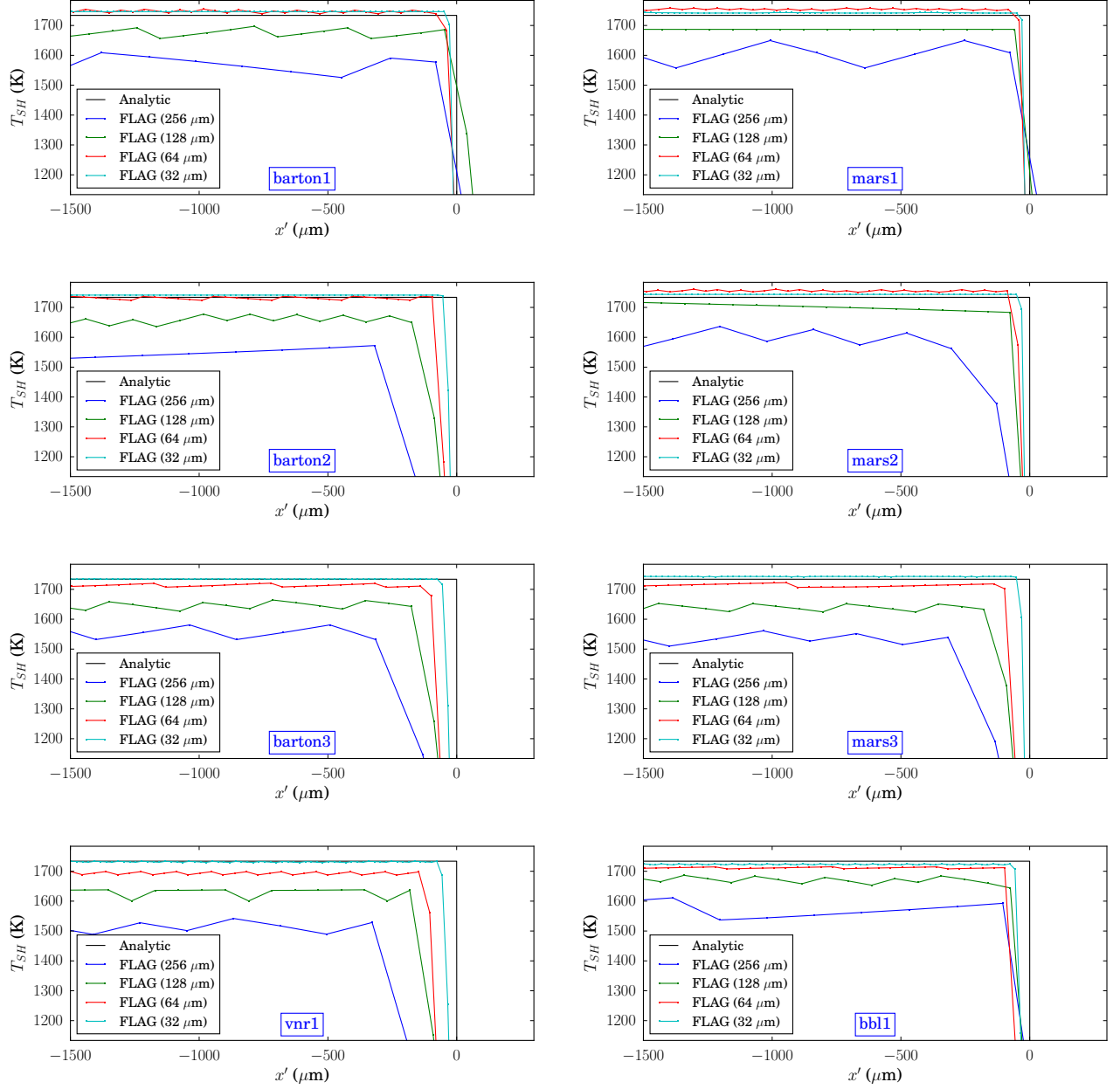


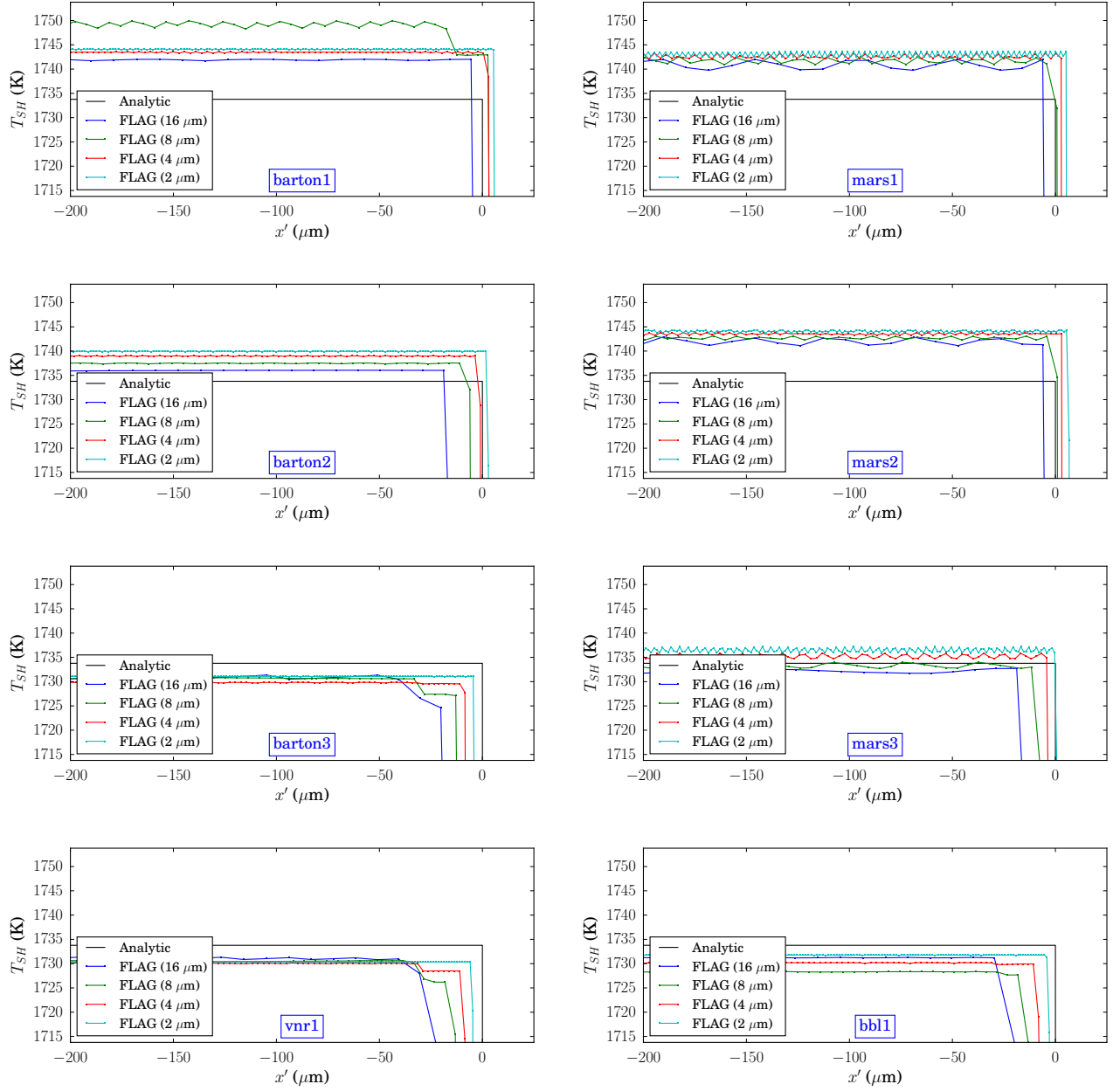
Figure 6.9: Convergence of shock pressure in SURFplus with *barton1*.

and equal to the shock temperature at  $\lambda = 0$ :

$$T^* = T[1 - a_T \lambda \exp(T_c/T)]. \quad (13)$$

Here,  $a_T$  and  $T_c$  are parameters which are chosen to keep  $T^*$  nearly constant through the early part of the reaction zone, but must also be calibrated to HE experiments with a range of initial temperatures (and corresponding shock temperatures). This approximation procedure for  $T_{SH}$  appears to cause AWSD to be more sensitive to the hydro code numerics (hydro scheme and artificial viscosity models).  $T_{SH}$  fields from AWSD for all AV models are shown in Figures 6.10 and 6.11. The predicted  $T_{SH}$  can be highly oscillatory for coarse resolutions. For fine resolutions in Figure 6.11, the axis limits are set for a narrower range near the exact  $T_{SH}$  value. We observe that the convergence of  $T_{SH}$  is **highly** dependent on the AV model and parameter choice. With increasing mesh resolution, most AV sets over-predict  $T_{SH}$  by a fraction of a percent leading to a  $D_{\text{sim}}$  that is higher than  $D_{CJ}$ . The AV sets which under-predict  $T_{SH}$  and  $D_{\text{sim}}$  are those that are more dissipative (i.e. *barton3*, *vnrl*, and *bbl1*).

Figure 6.10: AWS D  $T_{SH}$  profiles with coarse resolutions (256 - 32  $\mu\text{m}$ ).

Figure 6.11: AWS D  $T_{SH}$  profiles for fine resolutions (16 - 2  $\mu\text{m}$ ).

## 7 Additional results for selected AV model sets

Based on the previous analysis and comparison of AV models it is reasonable to eliminate some of the model/parameter sets. Subsequently, we will only investigate the “best” identified parameter set for each AV model. These are: *mars2*, *barton3*, *vnr1*, and *bbl1*. A full set of results for each burn model with the *barton3* AV set are given in Appendices D, E, and F. This includes plots for each variable at coarse resolutions (256 - 32  $\mu\text{m}$ ) and fine resolutions (16 - 2  $\mu\text{m}$ )

### 7.1 $L^1$ errors and rate of convergence

$L^1$  mean absolute errors are used to determine the rate of convergence (RoC) with grid refinement.  $L^1$  errors are calculated at  $t_{\text{stop}}$  as,

$$L^1 = \frac{\sum_{i=1}^n (|y_e - y_s| \Delta x)_i}{\sum_{i=1}^n (\Delta x)_i} \quad (14)$$

where  $y_e$  are the semi-analytic ZND solution data (interpolated to simulation spatial data),  $y_s$  are simulation data with points  $i$ , and  $\Delta x$  is the interval between spatial data points. The portion of the FLAG domain outside of the analytic solution (i.e.  $x < x_{\text{left}}$  after shifting) is not used for the  $L^1$  error calculation. Note that with Lagrangian calculations the zone size  $\Delta x$  is not constant at  $t_{\text{stop}}$ . The  $L^1$  errors are calculated for the hydrodynamic flow variables for each resolution. In Figure 7.1,  $L^1$  errors are plotted against resolution for  $\rho$  and  $e$ . The RoC is determined from a least-squares curve fit to the function:

$$\ln(L^1) = \ln(C) + \text{RoC} \ln(\Delta x_0) \quad (15)$$

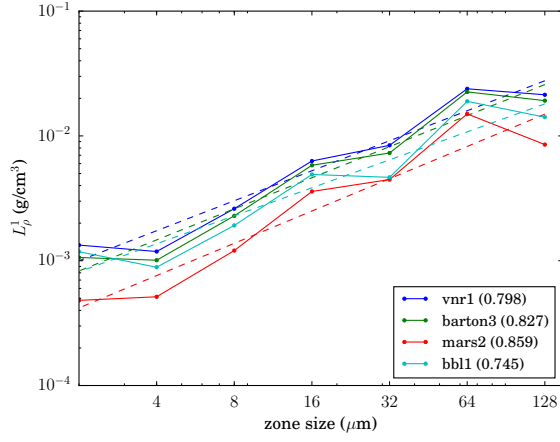
where  $\Delta x_0$  is the initial zone size.

We observe that trends in  $L^1$  errors from  $\rho$  and  $e$  are similar for a given burn model. The RoC values are typically between 0.7 and 0.9, indicating a first order convergence. However, MARS has significantly more deviation in the  $L^1$  errors with resolution which causes lower RoC values. In all of the models, there are unexplained kinks in the  $L^1$  trends where increasing resolution does not consistently reduce the errors.

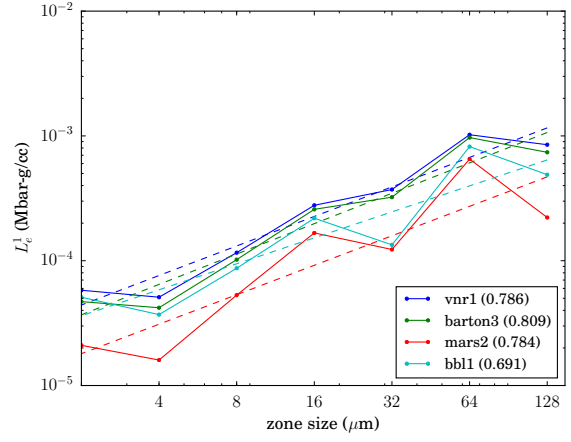
### 7.2 Model run times

It is interesting to compare computational cost between the burn models, AV models, and mesh resolutions. Some simulation details and run times are given in Tables 7.1 - 7.3. The main caveat being that these results are specific to the 1D ZND problem. Keep in mind that domain sizes were slightly different for each burn model setup (due to variation in the ZND reaction zone lengths), so the number of zones is not constant. A couple of things stand out from these results. First, the MARS simulations have the longest run times (1.4 - 1.9 times longer than the other AV models) for each burn model. Second, simulations with WSD and AWSO have much longer run times

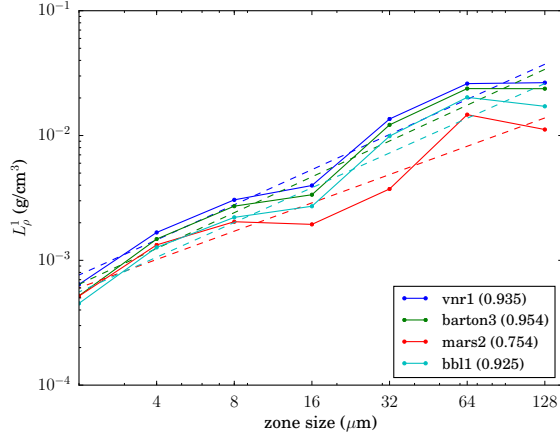




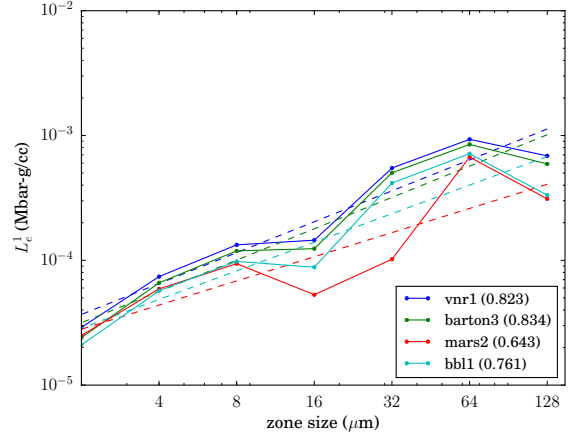
(a) WSD: density



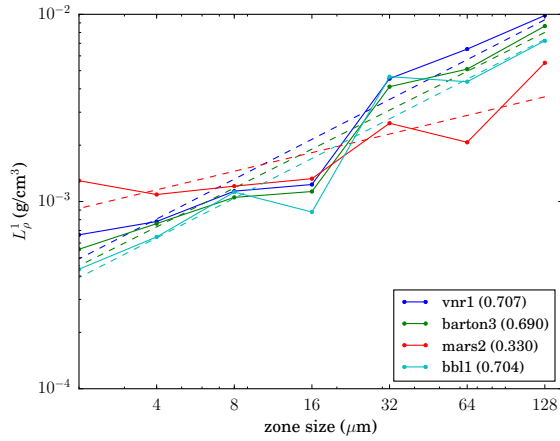
(b) WSD: energy



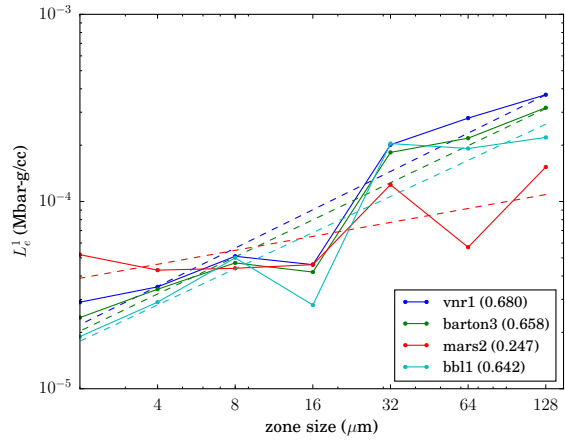
(c) SURFplus: density



(d) SURFplus: energy



(e) AWSD: density



(f) AWSD: energy

Figure 7.1:  $L^1$  errors from density and energy for the burn models. The dashed lines are fits to the errors with RoC values for the fits in parenthesis.

Table 7.1: WSD simulations: number of zones, number of processors, and run times.

zone size ( $\mu\text{m}$ )	no. zones	no. proc	run times (min)			
			<i>barton3</i>	<i>vnr1</i>	<i>mars2</i>	<i>bbl1</i>
256	245	1	0.053	0.052	0.107	0.064
128	490	1	0.177	0.170	0.351	0.218
64	980	2	0.465	0.455	0.873	0.565
32	1964	4	1.311	1.309	2.226	1.505
16	3924	9	4.219	4.167	5.948	4.490
8	7847	19	13.40	13.35	17.21	14.09
4	15720	30	41.04	40.68	51.06	43.16
2	31410	30	162.81	161.58	200.32	170.63

Table 7.2: SURFplus simulations: number of zones, number of processors, and run times.

zone size ( $\mu\text{m}$ )	no. zones	no. proc	run times (min)			
			<i>barton3</i>	<i>vnr1</i>	<i>mars2</i>	<i>bbl1</i>
256	244	1	0.045	0.044	0.088	0.054
128	488	1	0.139	0.137	0.316	0.182
64	976	2	0.325	0.316	0.706	0.408
32	1956	4	0.706	0.681	1.527	0.880
16	3915	9	1.511	1.491	3.184	1.944
8	7828	19	3.558	3.510	7.087	4.386
4	15630	30	10.01	9.844	18.94	12.18
2	31260	30	39.07	38.65	72.22	47.49

than SURFplus (between two to five times longer). This is surprising because the SURFplus code algorithm is more complex than either WSD or AWSO (i.e. having a separate lead shock detection algorithm, multiple fitting forms, and longer code). Fortunately, this striking difference in run times between burn models is not observed in other 2D test cases and appears to be specific to the ZND problem.

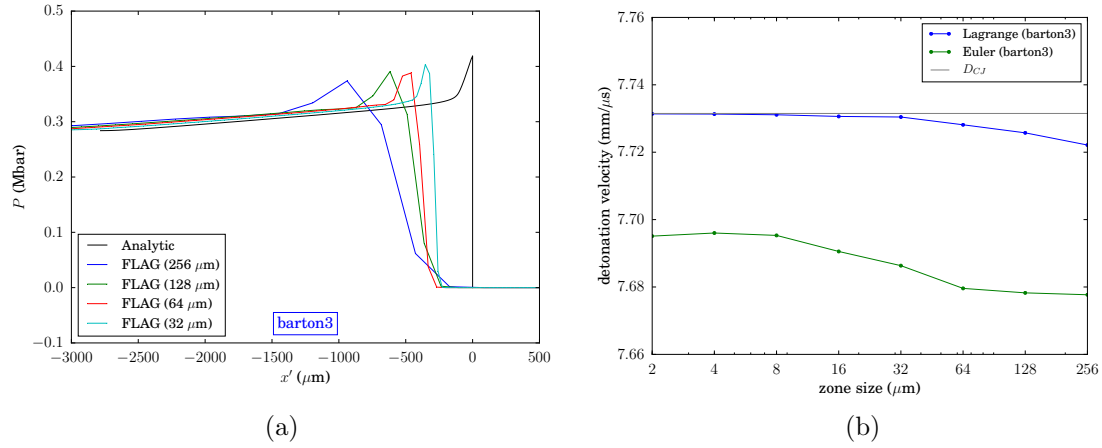
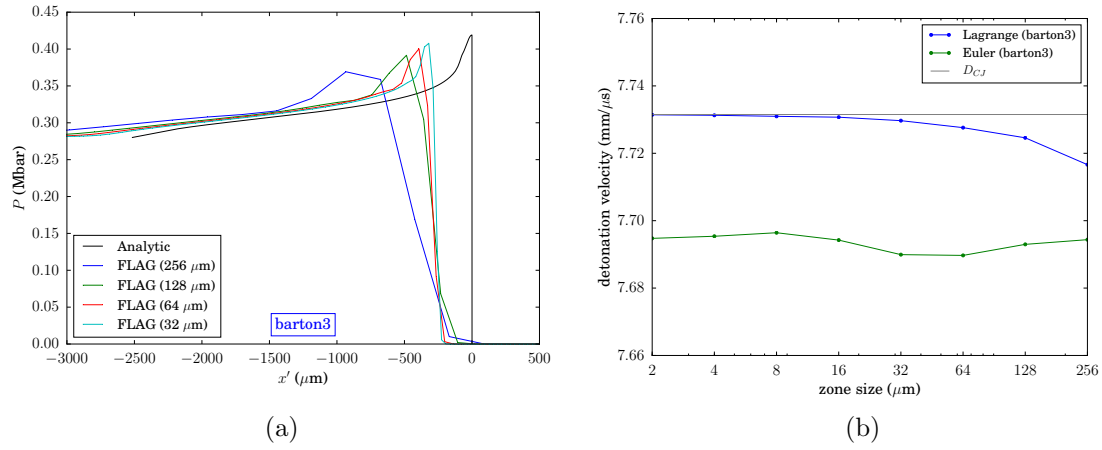
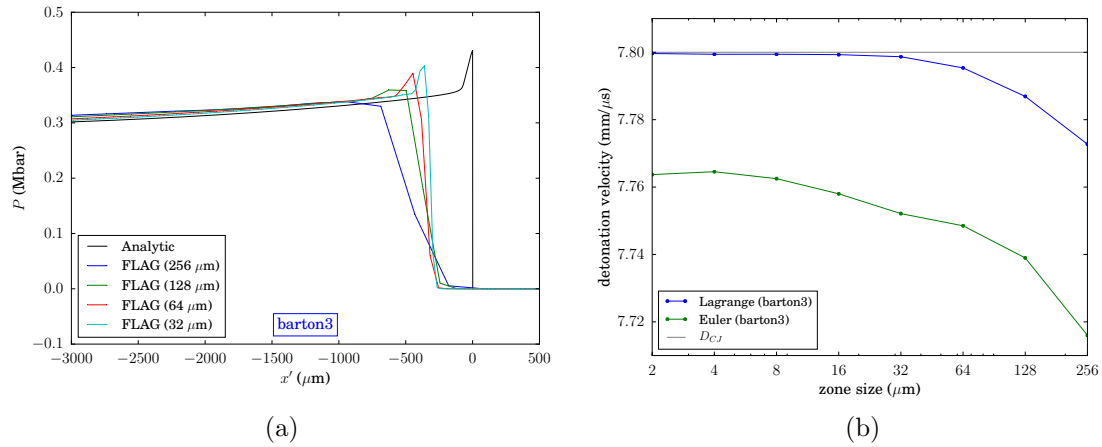
Table 7.3: AWSO simulations: number of zones, number of processors, and run times.

zone size ( $\mu\text{m}$ )	no. zones	no. proc	run times (min)			
			<i>barton3</i>	<i>vnr1</i>	<i>mars2</i>	<i>bbl1</i>
256	275	1	0.070	0.069	0.0120	0.081
128	550	1	0.248	0.255	0.451	0.299
64	1102	2	0.675	0.673	1.140	0.790
32	2205	5	1.794	1.774	2.712	1.989
16	4411	11	5.598	5.511	7.542	5.960
8	8822	22	15.72	15.50	19.63	16.54
4	17640	30	46.90	47.08	58.82	49.64
2	35280	30	189.13	186.54	232.71	196.05

## 8 Simulations with the Euler relaxer

All the simulations discussed so far have used a Lagrangian method (without ALE). Now we test the Euler ALE relaxer (with kinetic energy fixup). We choose the *barton3* AV set for this comparison because it had good convergence behavior in Lagrangian simulations. The simulation setup was identical to Lagrangian cases but with the addition of settings for ALE advection, the Euler relaxer parameters, and inflow boundary conditions (to ensure that density, energy, and velocity at the left side of the domain match the CJ state).

Pressure profiles from coarse resolution simulations and detonation velocity convergence for the burn models are shown in Figures 8.1 - 8.3. For all resolutions, the shock is distinctly too slow. The detonation velocities converge to values roughly 36 m/s less than  $D_{CJ}$  ( $\sim 0.5\%$  too low). The primary explanation for this is that ALE methods in FLAG are non-conservative. During remapping, internal energy is conserved but not kinetic and total energy [28]. The “kinetic energy fixup” attempts to correct this by offsetting internal energy into kinetic energy near shocks. The lack of convergence for the Euler ALE relaxer in FLAG is known to the code development team and is currently under investigation.

Figure 8.1: (a) Pressure profiles and (b)  $D_{\text{sim}}$  convergence for Euler simulations with WSD.Figure 8.2: (a) Pressure profiles and (b)  $D_{\text{sim}}$  convergence for Euler simulations with SURFplus.Figure 8.3: (a) Pressure profiles and (b)  $D_{\text{sim}}$  convergence for Euler simulations with AWSO.

## 9 Conclusions

This report has presented analyses of the propagating ZND detonation wave tests in PBX 9502 for verification of the WSD, SURFplus, and AWSO reactive burn models in FLAG. It was shown that all three models converge to the semi-analytic ZND solutions with increasing mesh resolution. AWSO has a slightly lower convergence rate and some difficulty converging to the exact detonation velocity compared with the other burn models (but still converges to  $\sim \pm 1$  m/s of  $D_{CJ}$ ). This is attributed to the sensitivity of the shock temperature approximation procedure in the AWSO model to numerical dissipation and oscillations near the shock. Simulations with the Euler ALE relaxer have detonation velocities that are too slow and do not converge to  $D_{CJ}$  due to non-conservation of energy.

The choice of artificial viscosity model and parameters has a strong influence on convergence for all three burn models, especially with coarser resolutions. The Barton model is directional but works well for this 1D case. However, the default parameters (*barton1* set) are not recommended for HE reactive burn simulations based on these ZND test and other validation tests. The VNR model performs satisfactorily when used with zonal aspect ratios close to unity. Simulations with MARS have longer run times than the other AV models, but often have lower  $L^1$  errors (particularly at coarser resolutions and with WSD and SURFplus). The BBL model is promising and should be tested more for larger more complex 2D problems. Each AV model investigated was able to provide adequate dissipation and good results when used with appropriate parameters. Based on these tests, recommended parameter sets for each AV model (Barton, VNR, MARS, and BBL) have been identified. It is recommended that these AV models and parameter sets be evaluated with more complex validation simulations (especially 2D). Future validation efforts could investigate shock initiation, over-driven shock initiation, propagating detonation (e.g. cylinder tests), shock diffraction (e.g. corner turning tests), and the effect of mesh orientation.

## References

- [1] W. Fickett and W. Davis, *Detonation*. Los Alamos series in basic and applied sciences, University of California Press, 1979.
- [2] M. Cowperthwaite, “An exact solution for axial flow in cylindrically symmetric, steadystate detonation in polytropic explosive with an arbitrary rate of decomposition,” *Physics of Fluids*, vol. 6, no. 3, pp. 1357–1378, 1994.
- [3] J. M. Powers and T. D. Aslam, “Exact solution for multidimensional compressible reactive flow for verifying numerical algorithms,” *AIAA Journal*, vol. 44, no. 2, pp. 337–344, 2006.
- [4] R. Menikoff, “Verification test of the SURF and SURFplus models in xRage: Part III affect of mesh alignment,” tech. rep., Los Alamos National Laboratory, LA-UR-16-26317, Aug 2016.

- 
- [5] B. L. Wescott, D. S. Stewart, and W. C. Davis, “Equation of state and reaction rate for condensed-phase explosives,” *Journal of Applied Physics*, vol. 98, no. 5, p. 053514, 2005.
  - [6] R. Menikoff and M. S. Shaw, “Reactive burn models and ignition & growth concept,” *EPJ Web of Conferences*, vol. 10, p. 00003, 2010.
  - [7] R. Menikoff and M. S. Shaw, “The SURF model and the curvature effect for PBX 9502,” *Combustion Theory and Modelling*, vol. 16, no. 6, pp. 1140–1169, 2012.
  - [8] T. D. Aslam, “Shock temperature dependent rate law for plastic bonded explosives,” *Journal of Applied Physics*, vol. 123, no. 14, p. 145901, 2018.
  - [9] R. Menikoff, “Verification test of the SURF and SURFplus models in xRage,” tech. rep., Los Alamos National Laboratory, LA-UR-16-23636, May 2016.
  - [10] R. Menikoff, “Verification Test of the SURF and SURFplus Models in xRage: Part II,” tech. rep., Los Alamos National Laboratory, LA-UR-16-24352, Jun 2016.
  - [11] V. H. Whitley, K. L. Stalsberg, B. L. Reichelt, and S. J. Shipley, “Model comparisons of the reactive burn model SURF in three ASC codes,” tech. rep., Los Alamos National Laboratory, LA-UR-18-20259, Jan 2018.
  - [12] C. E. Johnson, R. P. McCombe, and K. Carver, “A preliminary assessment of the SURF reactive burn model implementation in FLAG,” tech. rep., Los Alamos National Laboratory, LA-UR-17-28450, Sep 2017.
  - [13] M. A. Price, T. D. Aslam, and J. J. Quirk, “Validation of the AWSD reactive flow model with PBX 9502 experiments,” in *16th Symposium (International) on Detonation*, 2018.
  - [14] M. A. Price, “A study of shock initiation experiments for the explosive PBX 9502 using three reactive burn models,” in *21st Biennial Conference of the APS Topical Group on Shock Compression of Condensed Matter (SHOCK19)*, 2019.
  - [15] J. M. Powers, *Combustion Thermodynamics and Dynamics*. Cambridge University Press, 2016.
  - [16] E. L. Lee and C. M. Tarver, “Phenomenological model of shock initiation in heterogeneous explosives,” *The Physics of Fluids*, vol. 23, no. 12, pp. 2362–2372, 1980.
  - [17] R. Menikoff, “Shock Detector for SURF model,” tech. rep., Los Alamos National Laboratory, LA-UR-16-20116, Jan 2016.
  - [18] B. L. Wescott, D. S. Stewart, and W. C. Davis, “Modeling diffraction and dead zones in PBX-9502,” in *13th Symposium (International) on Detonation*, 2006.
  - [19] D. E. Burton, “Multidimensional discretization of conservation laws for unstructured polyhedral grids,” tech. rep., Lawrence Livermore National Laboratory, UCRL-JC-118306, Aug 1994.

- 
- [20] J. Von Neumann and R. D. Richtmyer, “A method for the numerical calculation of hydrodynamic shocks,” *Journal of Applied Physics*, vol. 21, no. 3, pp. 232–237, 1950.
- [21] R. Landshoff, “A numerical method for treating fluid flow in the presence of shocks,” tech. rep., Los Alamos Scientific Laboratory, LA-1930, Jan 1955.
- [22] L. G. Margolin, “A centered artificial viscosity for cells with large aspect ratio,” tech. rep., Lawrence Livermore National Laboratory, UCRL-53882, Aug 1988.
- [23] J. Campbell and R. Vignjevic, “Artificial viscosity methods for modelling shock wave propagation,” in *Predictive Modeling of Dynamic Processes: A Tribute to Professor Klaus Thoma* (S. Hiermaier, ed.), pp. 349–365, Boston, MA: Springer US, 2009.
- [24] M. L. Wilkins, “Use of artificial viscosity in multidimensional fluid dynamic calculations,” *Journal of Computational Physics*, vol. 36, no. 3, pp. 281 – 303, 1980.
- [25] N. R. Morgan, K. N. Lipnikov, D. E. Burton, and M. A. Kenamond, “A Lagrangian staggered grid Godunov-like approach for hydrodynamics,” *Journal of Computational Physics*, vol. 259, pp. 568 – 597, 2014.
- [26] N. R. Morgan. Private Communication, 2015.
- [27] R. L. Gustavsen, S. A. Sheffield, and R. R. Alcon, “Measurements of shock initiation in the tri-amino-tri-nitro-benzene based explosive PBX 9502: Wave forms from embedded gauges and comparison of four different material lots,” *Journal of Applied Physics*, vol. 99, no. 11, p. 114907, 2006.
- [28] J. L. Hill, “(U) User’s Manual for FLAG version 3.7.0,” tech. rep., Los Alamos National Laboratory, LA-CP-18-20066, Feb 2018.
- [29] J. Campbell and M. Shashkov, “A tensor artificial viscosity using a mimetic finite difference algorithm,” *Journal of Computational Physics*, vol. 172, no. 2, pp. 739 – 765, 2001.
- [30] R. Menikoff, “Errors when shock waves interact due to numerical shock width,” *SIAM J. Sci. Comput.*, vol. 15, p. 12271242, Sept. 1994.
- [31] R. Menikoff, “SURFplus Model Calibration for PBX 9502,” tech. rep., Los Alamos National Laboratory, LA-UR-17-31015, Dec 2017.

## Appendix A WSD model parameters

The WSD model implementation in FLAG follows the ignition and growth model form. Parameter names are different, but derived from, parameters in the original reference [5]. Parameters for PBX 9502 are given in the following tables.

Table A.1: Davis reactants EOS.

Parameter	Value	Units
<b>rho0</b>	1.895	$\text{g/cm}^3$
<b>t0</b>	293.0	K
<b>e0</b>	0.03731	$\text{Mbar}\cdot\text{cm}^3/\text{g}$
<b>a</b>	0.175	$\text{cm}/\mu\text{s}$
<b>b</b>	5.200	
<b>c</b>	0.100	
<b>z</b>	0.3093	
<b>cv0</b>	9.79e-6	$\text{Mbar}\cdot\text{cm}^3/\text{g}\cdot\text{K}$
<b>gamma0</b>	0.8168	
<b>alphast</b>	0.7331	

Table A.2: Davis products EOS.

Parameter	Value	Units
<b>a</b>	0.8592	
<b>k</b>	1.3000	
<b>n</b>	2.5210	
<b>vc</b>	0.9884	$\text{cm}^3/\text{g}$
<b>pc</b>	0.01307	Mbar
<b>b</b>	0.5800	
<b>cvp</b>	7.25e-6	$\text{Mbar}\cdot\text{cm}^3/\text{g}\cdot\text{K}$

Table A.3: WSD rate model.

Parameter	Value	Units
<b>rho0</b>	1.895	$\text{g/cm}^3$
<b>ra</b>	0.214	
<b>rb</b>	0.667	
<b>rc</b>	1.000	
<b>rd</b>	0.333	
<b>re</b>	0.500	
<b>rk</b>	892.86	$1/\mu\text{s}$
<b>rn</b>	2.000	
<b>ri</b>	1.0e5	$1/\mu\text{s}$
<b>rg1</b>	9223.8	$1/\text{MBar}^y \mu\text{s}$
<b>rg2</b>	3.036	$1/\text{MBar}^z \mu\text{s}$
<b>rlswtch</b>	0.9	
<b>rx</b>	7.00	
<b>ry</b>	4.50	
<b>rz</b>	1.00	
<b>rhoc</b>	2.74	$\text{g/cm}^3$

Table A.4: WSD deadening.

Parameter	Value	Units
<b>rkdead</b>	75.0	$1/\mu\text{s}$
<b>rpmax</b>	0.06	Mbar
<b>rphe1</b>	0.0007	Mbar



## Appendix B SURFplus model parameters

The SURFplus model parameters (fitting form 4) for PBX 9502 are taken from [31]. For the ZND tests an energy offset of  $e_0 = 0.0373204$  Mbar-cm<sup>3</sup>/g is used instead of the value reported in [5]. This is necessary to match the energy offset calculated (via EOSlib) in the ZND solution from Ralph Menikoff. SURFplus was calibrated with tabular EOSs and not the analytic Davis EOSs. Switching to Davis EOSs will causes the products Hugoniot without carbon clustering to cross the shock locus below the VN spike point. To avoid this, Menikoff choose to set  $q$  to half the value given in [31] for the ZND solution.

Table B.1: Davis reactants EOS.

Parameter	Value	Units
rho0	1.895	g/cm <sup>3</sup>
t0	293.0	K
e0	0.0373204 <sup>a</sup>	Mbar-cm <sup>3</sup> /g
a	0.175	cm/ $\mu$ s
b	5.200	
c	0.100	
z	0.3093	
cv0	9.79e-6	Mbar-cm <sup>3</sup> /g-K
gamma0	0.8168	
alphast	0.7331	

<sup>a</sup>set to match EOSlib value.

Table B.2: Davis products EOS.

Parameter	Value	Units
a	0.8592	
k	1.3000	
n	2.5210	
vc	0.9884	cm <sup>3</sup> /g
pc	0.01307	Mbar
b	0.5800	
cvp	7.25e-6	Mbar-cm <sup>3</sup> /g-K

Table B.3: SURF rate model (FF4).

Parameter	Value	Units
p0	6.0	
plow	8.0	
p1	28.0	
phigh	60.	
c	4.6e-5	
fn	4.05	
n	3.2	
nphi	0.0	
s1	2.0	
pburn	0.15	Mbar

Table B.4: SURFplus carbon clustering.

Parameter	Value	Units
q	0.015 <sup>a</sup>	Mbar-cm <sup>3</sup> /g
nratio	50	
t1	0.005	
t2	0.4	
h1	0.001	
h2	0.95	

<sup>a</sup>different from [31] but used for the ZND solution with Davis EOSs.

## Appendix C AWSO model parameters

The AWSO model parameters for PBX 9502 are from [8].

Table C.1: Davis reactants EOS.

Parameter	Value	Units
<b>rho0</b>	1.890	g/cm <sup>3</sup>
<b>t0</b>	297.0	K
<b>e0</b>	0.04115	Mbar-cm <sup>3</sup> /g
<b>a</b>	0.180	cm/ $\mu$ s
<b>b</b>	4.6	
<b>c</b>	0.34	
<b>z</b>	0.0	
<b>cv0</b>	1.074e-5	Mbar-cm <sup>3</sup> /g-K
<b>gamma0</b>	0.56	
<b>alphast</b>	0.4265	

Table C.2: Davis products EOS.

Parameter	Value	Units
<b>a</b>	0.798311	
<b>k</b>	1.35	
<b>n</b>	2.66182	
<b>vc</b>	0.75419	cm <sup>3</sup> /g
<b>pc</b>	0.032	Mbar
<b>b</b>	0.58	
<b>cvp</b>	1.072e-5	Mbar-cm <sup>3</sup> /g-K

Table C.3: AWSO rate model.

Parameter	Value	Units
<b>np</b>	0.5471	
<b>ps</b>	0.276	Mbar
<b>k1</b>	336.0	$\mu$ s <sup>-1</sup>
<b>t1</b>	1724.0	K
<b>a1</b>	0.06081	
<b>b1</b>	2.122	
<b>k2</b>	10200.0	$\mu$ s <sup>-1</sup>
<b>t2</b>	6278.0	K
<b>b2</b>	0.9	
<b>fs</b>	0.03587	
<b>lamc</b>	0.8764	
<b>diam</b>	0.02168	

Table C.4: AWSO rate model (additional parameters).

Parameter	Value	Units
<b>at</b>	0.327	
<b>tc</b>	971.0	K
<b>pzeta</b>	0.006	Mbar
<b>kzeta</b>	20.0	$\mu$ s <sup>-1</sup>

## Appendix D ZND test results for WSD with *barton3* AV set

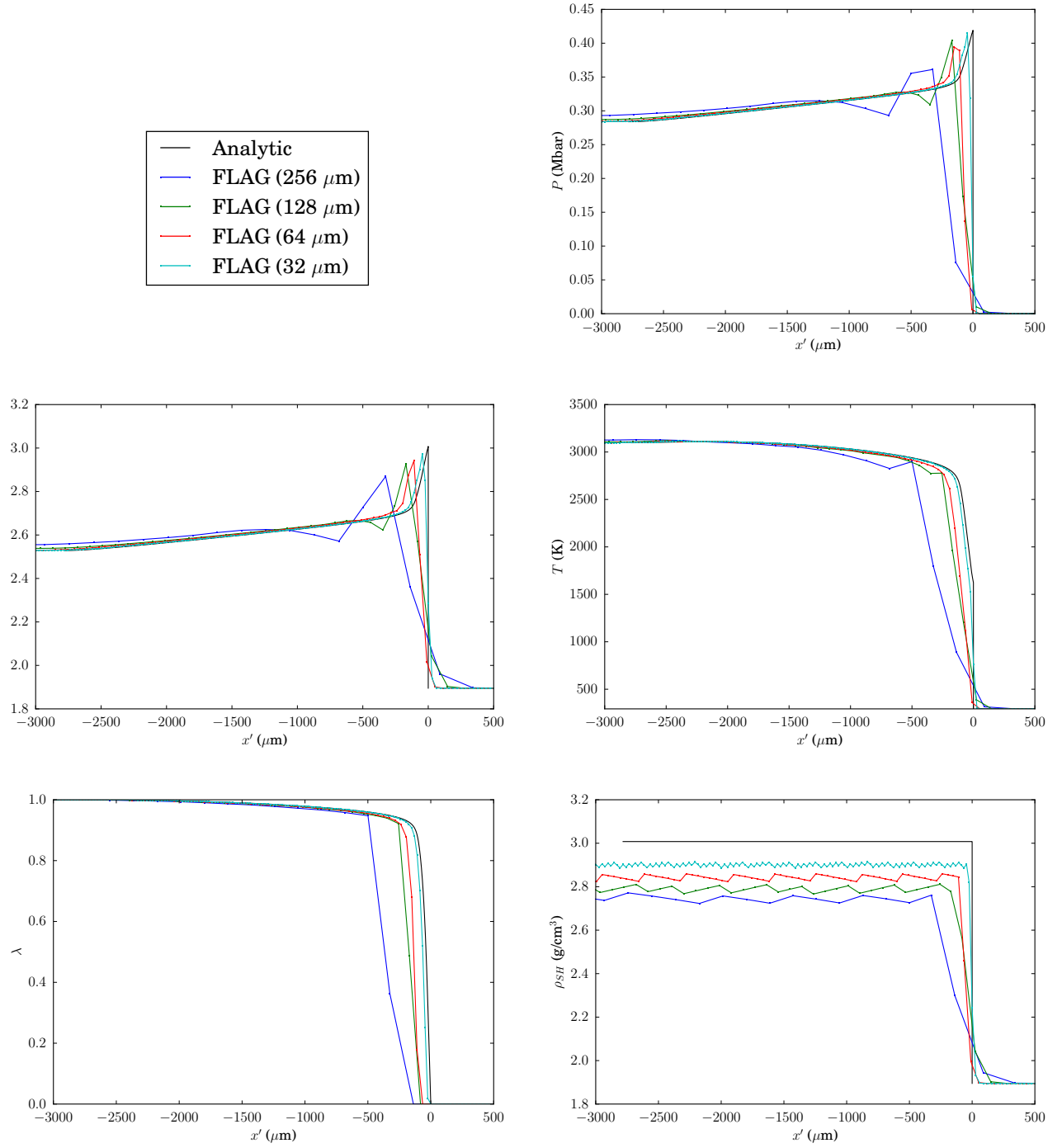


Figure D.1: Profiles for coarse resolutions (WSD).

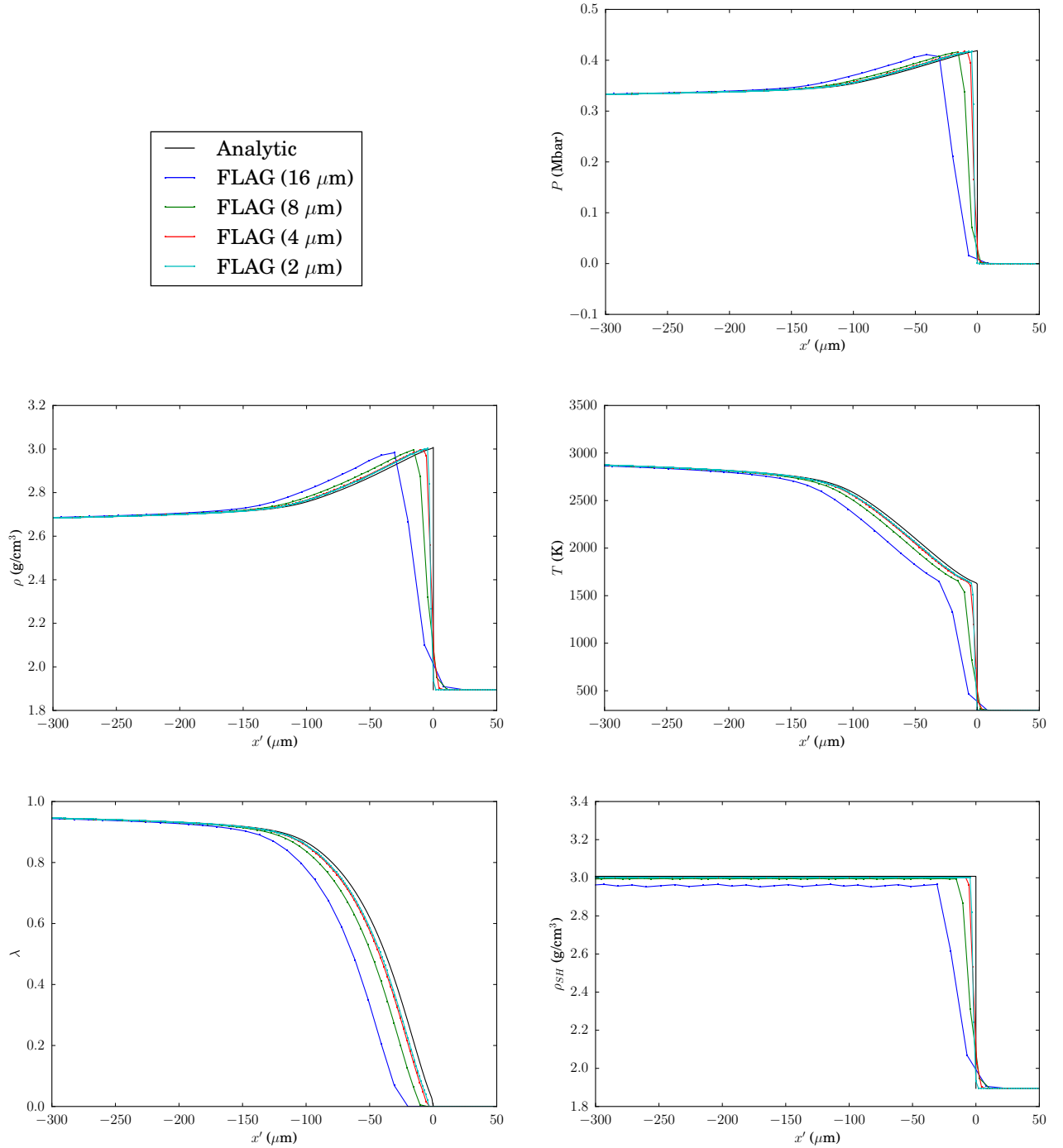


Figure D.2: Profiles for fine resolutions (WSD).

## Appendix E ZND test results for SURFplus with *barton3* AV set

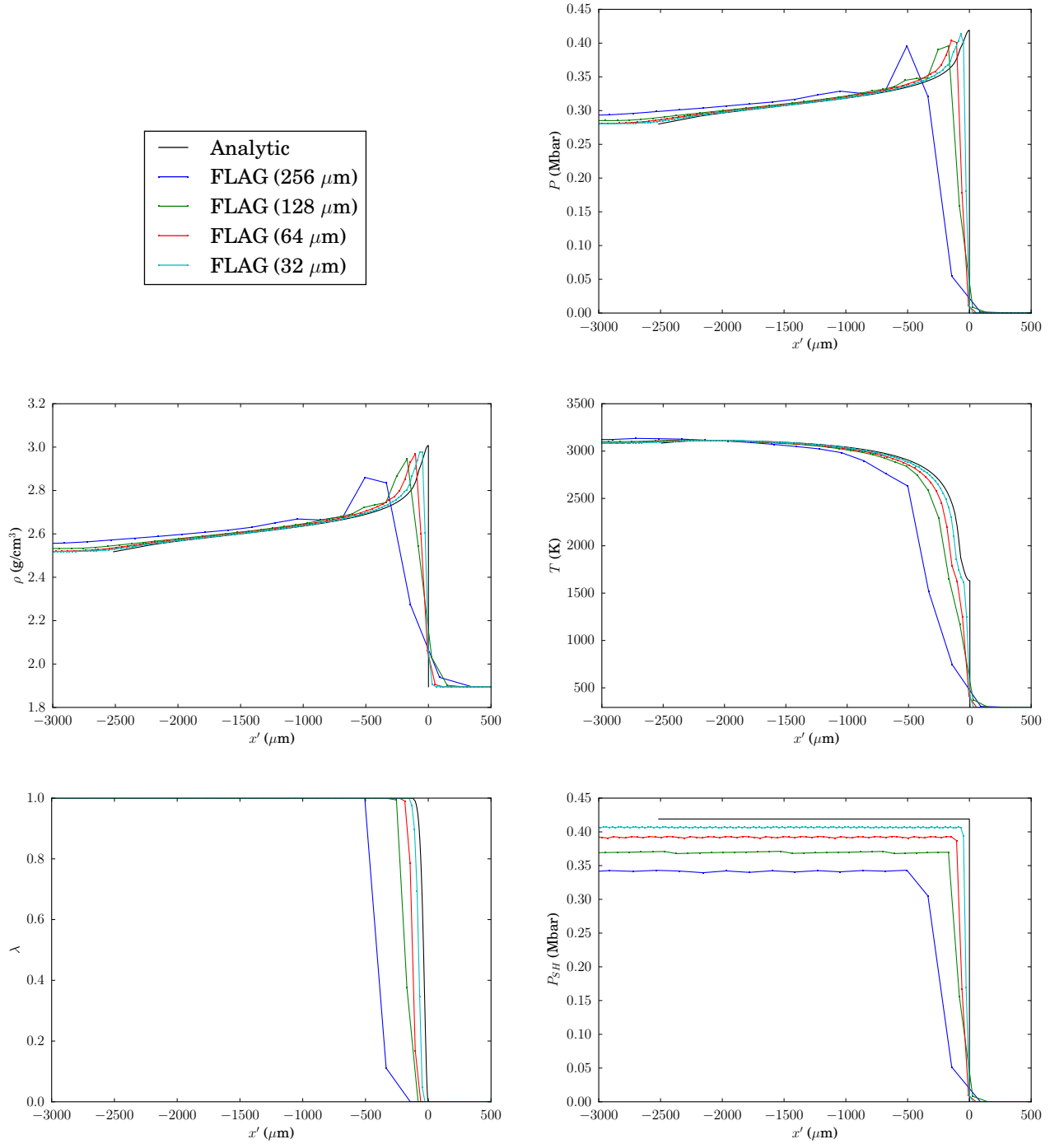


Figure E.1: Profiles for coarse resolutions (SURFplus).

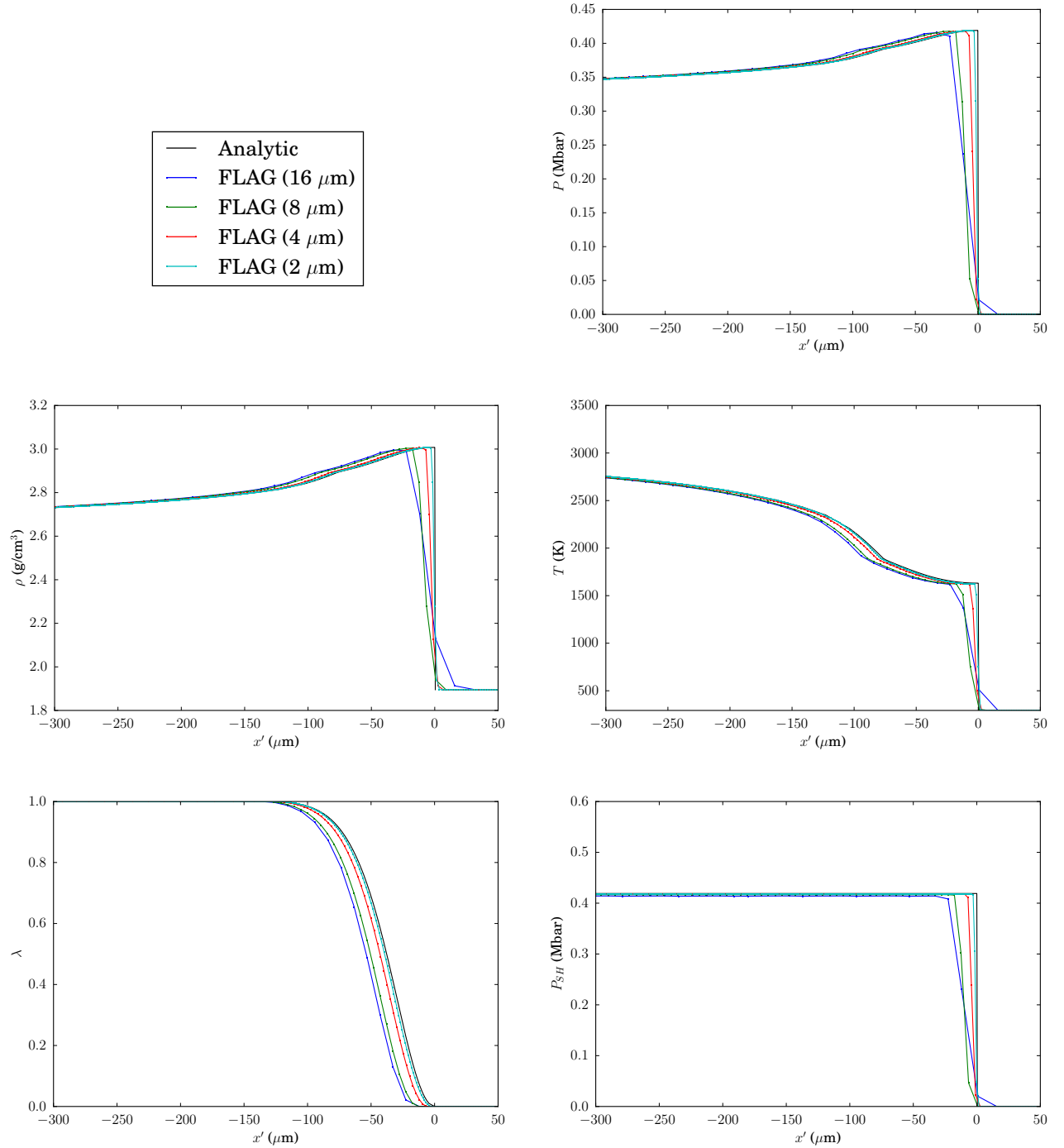


Figure E.2: Profiles for fine resolutions (SURFplus).

## Appendix F ZND test results for AWSO with *barton3* AV set

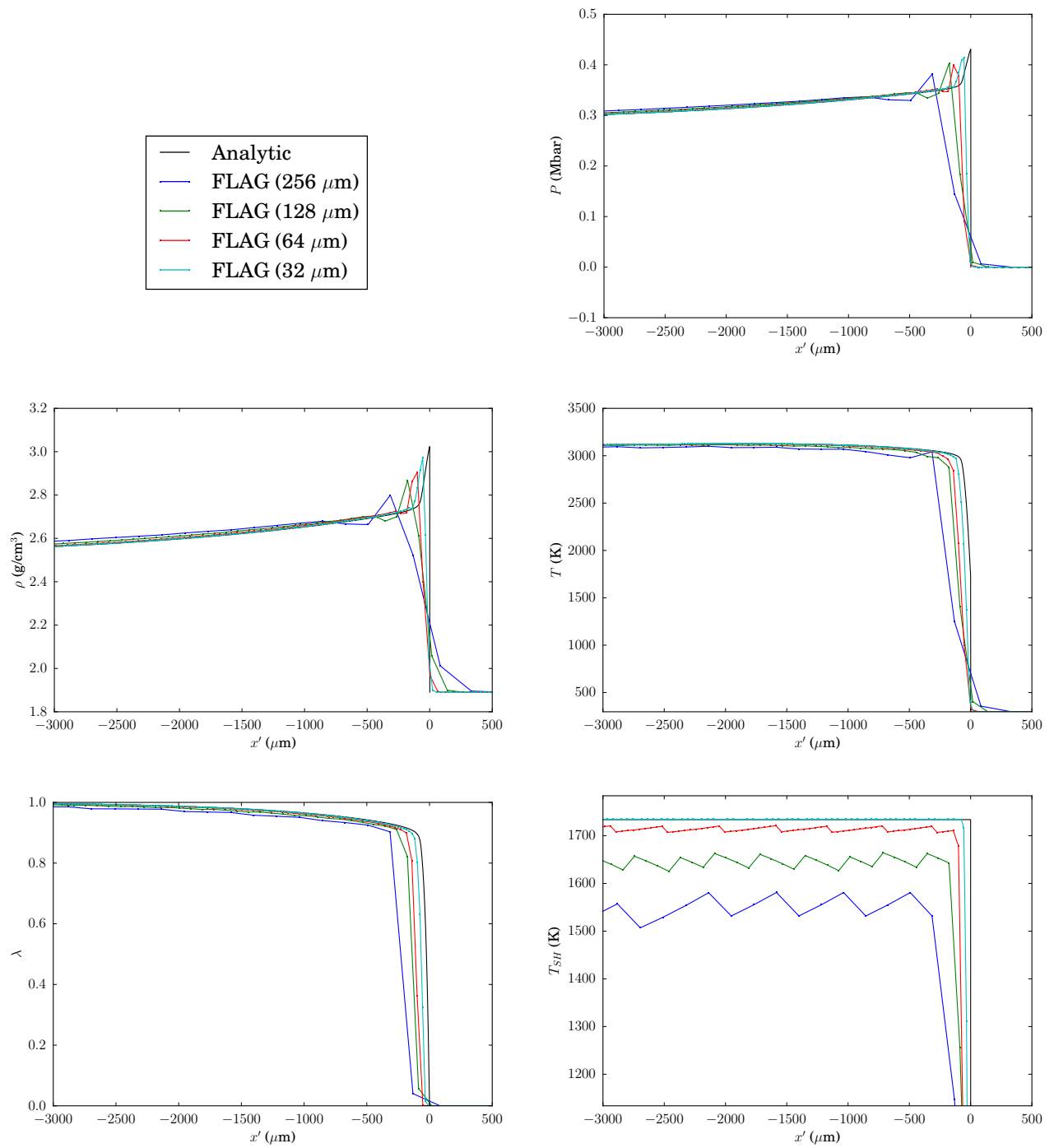


Figure F.1: Profiles for coarse resolutions (AWSO).

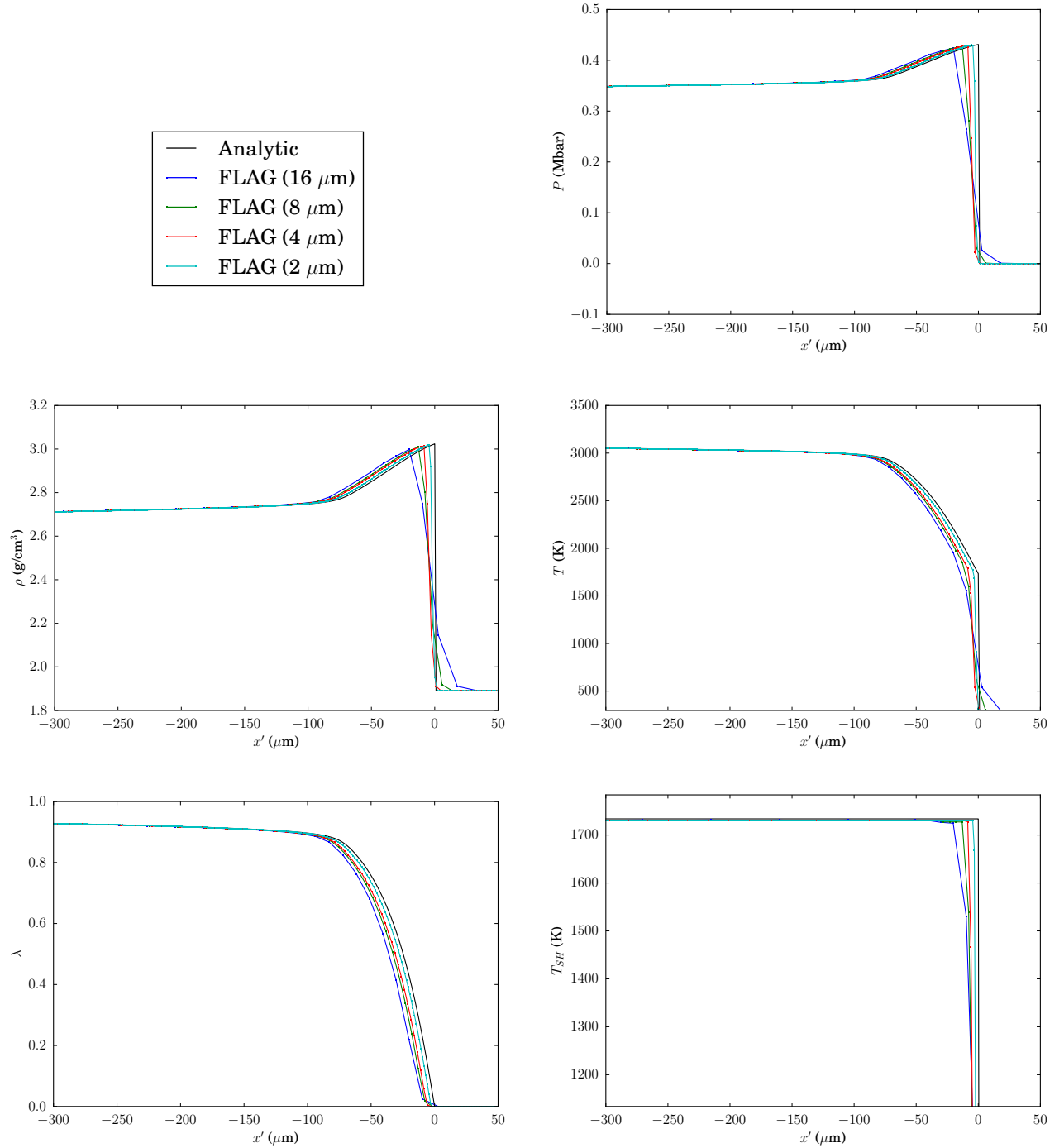


Figure F.2: Profiles for fine resolutions (AWSD).